Renewable Energy 224 (2024) 120057

Contents lists available at ScienceDirect

Renewable Energy

journal homepage: www.elsevier.com/locate/renene

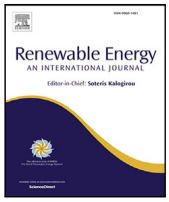

Analysis of spectral irradiance variation in northern Europe using average photon energy distributions

Basant Raj Paudyal [a,*], Sakthi Guhan Somasundaram [b], Atse Louwen [c], Angele H.M.E. Reinders [b,d], Wilfried G.J.H.M. van Sark [e], Dirk Stellbogen [f], Carolin Ulbrich [g], Anne Gerd Imenes [a]

[a] Department of Engineering Sciences, University of Agder, Jon Lilletuns vei 9, 4878 Grimstad, Norway
[b] Department of Design, Production and Management (DPM), University of Twente, De Horst, PO Box 217, 7500 AE Enschede, The Netherlands
[c] Institute for Renewable Energy, Eurac Research, Viale Druso 1, 39100 Bolzano, Italy
[d] Energy Technology Group, Eindhoven University of Technology, PO Box 513.5600 MB Eindhoven, The Netherlands
[e] Copernicus Institute of Sustainable Development, Utrecht University, Princetonlaan 8A, The Netherlands
[f] Zentrum für Sonnenenergie- und Wasserstoffforschung Baden-Württemberg (ZSW), Meitnerstr. 1, 70563 Stuttgart, Germany
[g] Helmholtz-Zentrum Berlin für Materialien und Energie, Hahn-Meitner-Platz 1, 14109 Berlin, Germany

ARTICLE INFO

Keywords:
Photovoltaics
Spectral irradiance
Average photon energy
Northern Europe
Clearness index

ABSTRACT

One major factor affecting the energy yield of photovoltaic modules is the spectral distribution of incident solar radiation. As spectral irradiance data is scarce, this study provides further documentation of recorded spectra at tilt angle 30°– 45° over a period from one to several years, with the resulting distributions of average photon energy (APE) in the 350–1050 nm wavelength range, from five locations in northern Europe. The results show a general trend of higher monthly APE values in summer and lower values in winter, with more pronounced APE variation at increasing latitude. Compared to the reference APE value of 1.88 eV, the largest variation in monthly APE is seen for the northernmost location of Grimstad, Norway, ranging from 1.82 eV to 1.93 eV between January and July with an annual average APE of 1.90 eV. The smallest variation is found for Merklingen, Germany, ranging from 1.86 eV to 1.88 eV between March and July, with an annual average APE of 1.86 eV. Comparing the annual average APE values of the various locations, the study shows a slightly blue-shifted spectrum for Berlin, Enschede and Grimstad, whereas Merklingen experiences a slightly red-shifted spectrum and the APE at Utrecht is similar to the standard reference spectrum. The simulations through SMARTS show air mass, water vapor and aerosols as the major parameters affecting the spectrum. During the winter months, distinct contributions from both clear and cloudy sky conditions result in a bi-modal APE distribution for all locations, which is not observed during the summer months. Analysis of APE demonstrates different site-specific behaviors, even though all sites are categorized in the same Köppen–Geiger (KG) climate class. These differences arise mainly due to atmospheric factors, whereas dissimilarity in albedo conditions, plane of tilt and instrumentation also have some contributions.

1. Introduction

As incident solar radiation enters the earth's atmosphere, it is significantly altered by various mechanisms until it reaches the surface. This has a direct impact on many scientific domains, including solar energy, meteorology, biology, atmospheric sciences and ecology, among others [1]. The growing deployment of photovoltaic (PV) technologies has made the precise performance rating of PV modules a matter of great concern for all the stakeholders. The characteristic parameters of PV modules are rated using standard test conditions (STC) given by 1000 W m^{-2} of irradiance, 25 °C of module temperature and an airmass AM1.5G spectrum [2]. Airmass is referred to as the relative path length of the photons through the atmosphere to the receiver at earth's surface [3]. For a zenith angle of 0° (mostly relevant for equatorial and tropical regions), the airmass is 1, i.e. AM1. The standard AM1.5G spectrum is the spectrum at the zenith angle of around 48° incident on a plane of 37° tilt with atmospheric conditions defined in ASTM G-173-03. The STC parameters of irradiance, temperature and spectrum constantly vary in outdoor measurements due to the dynamic nature of ambient conditions. Variation of even just a single STC parameter would incur a subsequent change in PV module performance.

Although the effects of broadband irradiance and temperature on PV performance have been extensively studied worldwide, the impact of

* Corresponding author.
E-mail address: basant.paudyal@uia.no (B.R. Paudyal).

https://doi.org/10.1016/j.renene.2024.120057
Received 22 May 2023; Received in revised form 9 November 2023; Accepted 24 January 2024
Available online 9 February 2024
0960-1481/

the varying solar spectral irradiance has not been explored to the same extent [4]. Precise information about the solar resource, including both broadband and spectral irradiance, is the basis for PV system design and estimation of the energy yield under specific weather conditions. Energy rating, which is a quantification of the electrical energy generated by the PV modules over time, is arguably more useful for long-term performance evaluation [5,6] of PV modules than the STC power rating currently used. Energy rating is aimed at characterizing the PV modules performance based on their location's specific energy yield, which subsequently will help the end users to decide on the optimal PV alternatives [7]. Moreover, investigating variations in the incident solar spectral irradiance is especially important for the development of new PV technologies. The impact of spectral variation on the single junction cells is generally known. PV devices with narrower spectral response (SR) (i.e., a-Si, CdTe) are more sensitive to such variation compared to the PV devices with wider spectral response (i.e., c-Si, CIGS, HIT) [8–10]. In case of a tandem solar cell the two subcells absorb a different part of the solar spectrum. The subcell generating the lower current limits the current through the tandem in a serial connected configuration. The voltages add up and the world record efficiency for such devices outperform single junction Si devices and have surpassed 30% efficiency [11]. A tuning of the bandgaps to a maximum power output is usually done under AM1.5G [12]. Any deviation of the incoming spectrum leads to a different share of the incoming photons between the two subcells and thus to losses. As the number of junctions increase, the sensitivity to the spectrum also increases and the corresponding overall efficiency increases [13].

Several research groups have been working on the analysis of solar spectral distribution analysis for PV applications across the world. For this purpose, researchers use various spectral indices to quantify the two-dimensional spectral irradiance (i.e., intensity as a function of wavelength) by a single parameter and analyze the impact on PV performance.

1.1. Spectral irradiance analysis

The reasoning behind using spectral indices is two-fold: firstly, to provide insights on spectral information, in view of the scarcity of spectral irradiance data, that can be applied more generally than just the single specific location of the measurement. Secondly, to accommodate for more efficient simulation purposes, since it is quite computationally intensive to use long time-series of high-resolution spectra to evaluate spectral effects on the PV module performance.

Some authors [8,14] collected the spectral irradiance data for several years and studied the spectral impact using the average photon energy (APE) [14] and useful fraction (UF) [15] as spectral indicators on mostly (but not limited to) thin-film modules. Whereas APE describes the incident solar irradiance distribution and depends on the wavelength interval selected for its calculation, UF is a device-specific parameter referring to the active wavelength region of a given PV material. Multiple years of spectral data and the subsequent impact on the PV parameters were presented in [6,16,17] where the authors used APE as an indicator in their studies and proposed a methodology to test its uniqueness in characterizing a solar spectrum [18]. Spectral influences using APE, the spectral factor (SF, also a device-specific parameter), and the reciprocal of SF (SF^{-1}), on PV performance were quantified through the performance ratio (PR) from measurements at several locations in Japan [19,20]. The spectral variation and its impact on various thin-film PV modules installed in tropical conditions were studied by [21] using APE and the effective irradiance ratio (EIR). [10] performed an analysis on the impact of spectral variations based on APE and UF for four different seasons in India. Similarly, [22] used APE to characterize the measured spectral irradiance in Rome, Italy.

The correlation between SF^{-1} and ambient conditions like humidity, barometric pressure and temperature was presented in [23]. Whereas temperature showed a positive correlation with SF^{-1}, humidity did not show any apparent correlation. In [24], results from a comparative study regarding the spectral impact on the energy yield of different PV technologies were presented for four sites in Europe, where the authors used SF for their analysis and found that the seasonal spread experienced by the spectral gains of high-bandgap materials gets smaller at lower latitudes. In [25], a worldwide analysis of 124 sites on the PV spectral factor for seven common PV technologies was presented, where the spectral irradiance was modeled at these locations using Simple Model for Atmospheric Transmission of Sunshine (SMARTS) spectral solar irradiance model [26]. From the results, a remarkable influence of water vapor content and a lower influence of aerosols, quantified in terms of aerosol optical depth (AOD) on the monthly spectral factor of thin film devices was observed.

Altogether, the studies from various locations point to the fact that APE is a good qualitative indicator of solar spectral variation, but it is not better than the spectral mismatch factor (MMF) when quantifying the PV yield [9] and its use for the quantification of instantaneous spectral impacts on PV performance is not recommended [20,27]. Nevertheless, APE is still a widely used parameter in PV applications to represent the solar spectral distribution as a single number. Several studies have shown that APE can be considered unique for results related to the specific dataset under scrutiny [17,28–30], while also pointing out that the question of uniqueness needs verification for other different climatic and geographical locations. Contrary to this, some researches have shown that an APE value can arise from multiple different spectra and therefore cannot be considered unique [7] or can only be considered statistically unique within the limits of the 450–900 nm wavelength range [31]. Compared to the other existing indices blue factor (BF), UF, and SF, the quantification of spectral distributions through APE involves lower uncertainty [32,33]. The spectral irradiance and subsequently APE depends on the geographical and meteorological conditions caused by the presence of aerosols, water vapor (from either clouds or humidity) and different gases (O_2, O_3, CO_2, etc.). In addition, local meteorological factors, like atmospheric pressure or ambient temperature, are also known to have an impact. Therefore, parameterizing the effects of such atmospheric factors known to influence APE is an important prerequisite to assess the variation in spectral distribution across different locations.

1.2. Spectral measurement techniques

Spectral irradiance distributions are measured by devices known as spectroradiometers. The general principle of these devices is to disperse the incident beam of light into its spectral components and measure the energetic content at various wavelengths. The availability of spectroradiometers depends on the required measurement range and usage in the technical field [34]. The spectral irradiance measurement is realized in two different ways; either by measuring the spectrum at every wavelength using wide-band spectroradiometers, or by measuring at a few specific wavelengths that are then incorporated into mathematical models to derive the full spectrum. The latter devices are known as multifilter radiometers.

For the traditional spectroradiometers, devices with a variable grating are known as rotating grating or scanning type spectroradiometers, while devices with a fixed grating and a linearly aligned detector array are known as array spectroradiometers. The earliest spectroradiometers operated on the scanning principle, where the scanning rate varied in a range from seconds to minutes depending upon the wavelength intervals [35]. Due to the scanning of each wavelength, the complete scan duration of these devices is long and they are unsuitable in cases requiring a faster measurement of spectral variation [36]. Although scanning-type spectroradiometers are accurate, they severely lag on measurement duration and are better suited to indoor laboratory purposes. Array-type spectroradiometers are the preferred devices in outdoor environments, especially in solar applications as seen in the

Table 1
Data set description for each participating site with all locations having KG climate classification of Cfb.

Parameters	Berlin	Enschede	Grimstad	Merklingen	Utrecht
Latitude (°N)	52.43	52.23	58.33	48.53	52.5
Longitude (°E)	13.52	6.85	8.58	9.71	5.10
Climate type	Urban, Inland	Sub-urban, Inland	Sub-urban, Coastal	Rural, Inland	Sub-urban, Inland
Spectral instrument	EKO WISER	EKO MS700	Spectrafy SolarSIM-G	EKO MS700	EKO MS700
Spectral range (nm)	300–1700	350–1050	280–4000	350–1050	350–1100
Time-series	2018–2021	2014–2019	2019–2021	2014–2020	2014–2017
Temporal resolution	5 min	1 min	1 min	1 min	30 s
Orientation (tilt, azimuth)	35°, S	30°, S	45°, S (173°)	40°, S	37°, S

last few decades [37–39], due to their fast data acquisition rates, portability, and compact size.

The multifilter radiometer approach was first presented as an idea by [40] to apply an extrapolation model to the extended wide range 300–4000 nm. Results were in good agreement with the total direct solar irradiance as measured with an absolute cavity radiometer. A multifilter radiometer equipped with six silicon photo-diodes with bandpass filters, measuring the spectral direct normal irradiance (DNI) in carefully chosen wavelength ranges, is presented in [41]. A similar device using nine photo-diodes (seven silicon and two indium gallium arsenide) to measure the spectral global horizontal irradiance (GHI) is presented in [42]. The measurements from both these devices are combined with mathematical models to determine atmospheric transmittance. These devices house a printed circuit board for data acquisition, measuring the photo-diode current from each filter channel along with temperature and pressure sensors [43]. These measurements are then processed by software that incorporates a model to reconstruct the solar spectrum in the full 280–4000 nm range. This results in the spectral irradiance distribution of irradiance under all-sky conditions.

1.3. Objective of this work

Overall, as spectral irradiance data is scarce owing to the high cost and complexity of the sensors and measurement setup, this study provides further documentation of recorded spectra over several years and the resulting distributions of APE values from five different locations in Northern Europe. Generally, Northern Europe experiences a higher share of diffuse sky conditions compared to regions in the South [44]. This study aims to investigate and quantify these spectral differences using APE as a single parameter. The novelty of this work lies in the comparison and analysis of spectral distributions across different locations from this part of the world, which is being reported for the first time. In Section 1, the general introduction to the work and literature review is presented. Section 2 contains a brief description of the measuring facilities at each location, quantification of the spectral variation using APE, and the methods employed to filter and analyze the data. Section 3 presents the effects of various atmospheric factors on APE and ultimately on spectral irradiance through simulated spectra in SMARTS and measured data. The impact of various factors on APE is analyzed, leading to the evaluation of the dependence of APE's monthly variations on sky conditions. Finally, the conclusions of this work are given in Section 4.

This project is a result of the joint collaboration under the EU COST Action PEARL-PV program with the target to improve the reliability and energy performance of PV systems in Europe [45].

2. Materials and methodology

2.1. Experimental details and data collection

Datasets of spectrally-resolved global irradiance in the plane of array (G_{POA}) have been obtained from five locations as shown in Fig. 1, using different instruments with different wavelength ranges under different climatic conditions, time-series and time resolution. Interestingly, the overall climatic conditions at each location are described

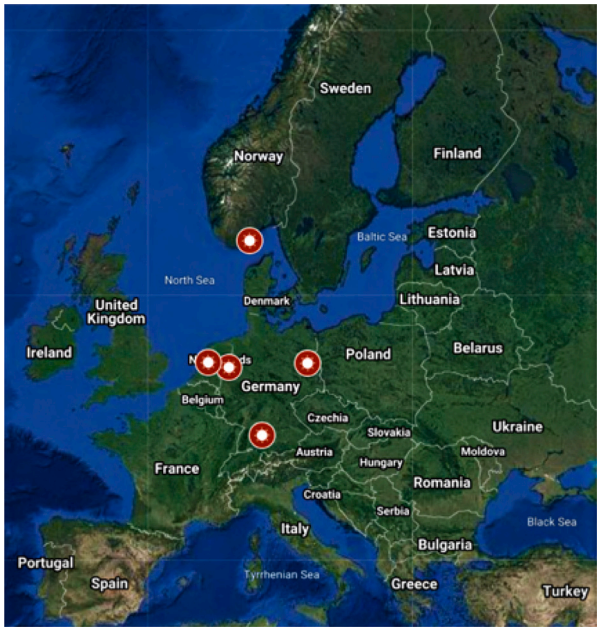

Fig. 1. Geographical representation of the participating locations of this study.

by the same KG climate classification (Cfb). The KG classification is widely accepted in climatology-related fields and describes the climate of any location with a single metric based on multiple variables and their seasonalities [46].

Four locations use an array-type spectroradiometer [37] whereas Grimstad uses a filter-type radiometer [42] combined with spectral modeling. Table 1 contains general information about the five participating locations in this study, in addition, a brief description of each site is provided in what follows.

2.1.1. Helmholtz-Zentrum Berlin, Germany

At the Helmholtz-Zentrum, Competence Centre Photovoltaics Berlin (PVcomB), the outdoor test facilities (52.43°N, 13.52°E) are designed to investigate the outdoor performance and operational stability of industrial and research cells and modules (among others, Perovskite-Silicon tandems). The foci of the research are device encapsulation, temperature coefficients, energy yield, verification of the indoor accelerated ageing tests, as well as data analysis techniques. The setup is appropriate to analyze the Maximum Power Point (MPP) tracking and I-V curves of differently sized samples and installations under varying non-ideal irradiance conditions. (The PV monitoring system for small cells and modules is supplied by the Laboratory of Photovoltaics and Optoelectronics of the University of Ljubljana, whereas a commercial product is used for industrial modules.) The data acquisition system also includes sensors installed on the PV facade, thus also supporting research on building integrated photovoltaics (BIPV). A weather station (from CLIMA SENSOR US/Adolf Thies GmbH & Co.) records the ambient temperature, wind speed, wind direction, humidity, air

Fig. 2. Part of the experimental setup at Helmholtz-Zentrum Berlin, Germany.

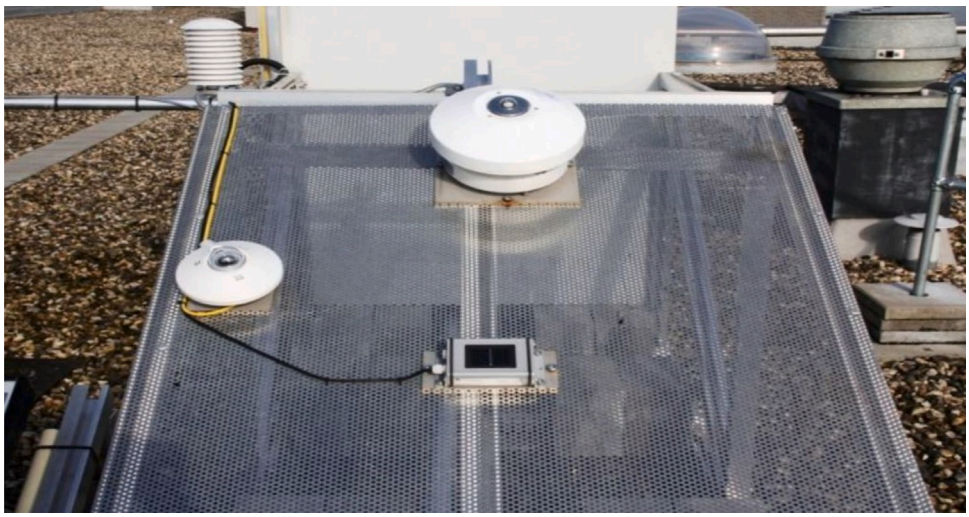

Fig. 3. Experimental setup at the University of Twente, Enschede, Netherlands.

pressure and precipitation intensity. Two Kipp and Zonen CMP 11 pyranometers measure global and diffuse irradiance (shadow ring) in the horizontal plane. The climate sensor and pyranometers are connected to an DLx MET datalogger from Adolf Thies GmbH & Co., and provides one minute averaged data. Two EKO WISER spectroradiometers, tilted at 35° and 90° as shown in Fig. 2, record the incident spectrum continuously every 5 min.

2.1.2. University of Twente, Enschede, Netherlands

At Enschede, the experimental data is constituted of irradiance spectra that were measured at the PV test bench facility located at the University of Twente in Enschede (52.23°N, 6.8°E). The datasets comprise spectrally-resolved one-minute irradiance measurements from 5:05 a.m. to 10:20 p.m. each day for the years 2014–2019. The CR1000 datalogger from Campbell Scientific with a built-in power source and memory was used to record the data, which was then transmitted to a data server at the University of Twente. The data was monitored with an EKO MS-700 spectroradiometer (Fig. 3) for the bandwidth range of 350 – 1050 nm with a wavelength interval of 1, 3, or 5 nm.

2.1.3. University of Agder, Grimstad, Norway

The experimental location at the University of Agder is in the coastal city of Grimstad, Norway (58.33°N, 8.58°E). Different PV technologies are installed on a south-facing open rack (tilt 45°, azimuth 173°) on top of a five-storey building 60 m above sea level, as shown in Fig. 4. Various environmental sensors are installed to measure the broadband and spectral irradiance, ground albedo, module and ambient temperatures, humidity, precipitation, air pressure, wind speed and wind direction. The broadband irradiance is measured horizontally and in the plane of array using CMP11 pyranometers from Kipp and Zonen, as well as mono-Si reference cells. The direct normal and diffuse horizontal irradiance components are measured using a CHP1 pyrheliometer and a CMP11 pyranometer with shading ball (mounted on a SOLYS2 tracker from Kipp and Zonen). Spectral irradiance is also measured in both planes by SolSIM-G multifilter radiometers from Spectrafy. These radiometers include seven silicon and two indium gallium arsenide photo-detectors combined with nine hard-coated narrow bandpass filters [42]. The current generated by the photo-detectors in these channels and additional ambient parameters measured by these devices are used as inputs to a proprietary radiative transfer model to derive estimates of the real-time spectral and broadband irradiances. The environmental parameters are recorded through a CRX1000 Datalogger from Campbell Scientific. Environmental data and irradiances are measured every minute and stored in a central database together with PV module I-V curves which are separately recorded. Solar spectra have been recorded at 1-min resolution between sunrise and sunset from October 2019 onwards.

Fig. 4. Experimental setup at the University of Agder in Grimstad, Norway.

Fig. 5. Aerial view of the ZSW test site Widderstall. The insert shows part of the meteorological measurement set-up including the EKO MS-700 spectroradiometer (second from left).

2.1.4. ZSW, Stuttgart, Germany

The ZSW (Zentrum für Sonnenenergie- und Wasserstoffforschung Baden-Württemberg) Widderstall PV test site is located in the municipality of Merklingen (48.54°N, 9.71°E) at 750 m above sea level. The facility is being operated since 1989 and comprises test beds for field-testing of PV modules with IV curve tracers by Papendorf, as well as PV systems with high-precision DC and AC electrical monitoring by Papendorf and Gantner Environmental Instruments. Further, the test site includes some specific test set-ups like rooftop and facade installations, one-axis trackers and a sun-tracking 3X-concentrator for accelerated aging in an outdoor environment. The weather monitoring includes multiple irradiation measurements (mostly Kipp and Zonen second-class pyranometers) as well as the recording of ambient temperature, pressure, humidity, wind speed and direction, and precipitation with LUFFT WS200 and WS500 integrated weather sensors. The spectral irradiance is measured by an EKO MS-700 spectroradiometer, which is mounted facing south at 40° tilt and in the same orientation as the fixed test racks for PV modules and systems (see insert in Fig. 5). The instrument delivers 1-minute records of the spectral irradiance in the range of 350 – 1050 nm from which datasets for the years 2014–2020 are available for the analysis in this paper.

2.1.5. UPOT, Utrecht, Netherlands

At the campus of Utrecht University (52.1°N, 5.2°E) spectral measurements are part of the Utrecht Photovoltaic Outdoor Test facility (UPOT) [4,47], see Fig. 6. The test facility is located at the top of an eight-storey building, at a height of about 36 m above sea level. The facility operates year round, 24 h per day, performing measurements on a set of more than 20 PV modules, with a variety of irradiance and atmospheric sensors. Measurements of PV module performance are performed at in-plane irradiance values above 50 W/m^2. Measurements of meteorological data, however, including spectra, are performed continuously. Modules are mounted at a tilt of 37° towards the South. Next to an EKO Instruments MP160 IV Curve tracer, several irradiance sensors (EKO Instruments pyranometers) are installed, mounted in plane with the modules as well as horizontally. The broadband direct and diffuse irradiance components are measured separately. For spectral measurements, the EKO MS700 spectroradiometer with 300–1100 nm measurement range is employed, installed in plane with the modules. The datasets comprise of spectrally-resolved 30–second irradiance measurements starting in July 2014 and ending in May 2017.

Fig. 6. Experimental setup at Utrecht University, Utrecht, the Netherlands. P denotes locations of pyranometers, S of the spectroradiometer.

2.2. Data preparation and filtering

The calculated value of APE and broadband integral irradiance are affected by the range of wavelengths over which they are computed. For the two different wavelength ranges 350 – 1050 nm and 350 – 1700 nm, the corresponding APE values for the AM1.5G reference spectrum are 1.88 eV and 1.59 eV, respectively. Since the unavailability of a commonly measured wavelength range can prevent the direct comparison of APE values between datasets from multiple locations [48], the range of 350–1050 nm is chosen as a common interval across all locations for this intercomparison.

As mentioned previously, the locations considered in this study exhibit a relatively large diffuse fraction in winter, which together with high solar zenith angles cause the average total broadband irradiance to remain low over extended periods of the year. The lowest broadband irradiance values are most affected by measurement uncertainty and small random deviations from noise in the signal, which introduce ambiguity in the data analysis and hence need to be filtered out. Filtering of datasets, however, is a non-trivial task because using the wrong filters could induce bias in the results. It is a challenging task in this work as well, whereby a higher threshold limit for broadband irradiance would exclude a large number of datasets from the winter season, whereas a lower threshold would include noisy data aided by measurement uncertainties. In order to include a sufficiently high number of data-points for the analysis, the irradiance threshold for discarding data is here set to 25 W m^{-2}, where datasets corresponding to irradiance lower than this threshold are not included in the analysis.

2.3. Data analysis methodology

The general methodology of the work includes the calculation of the APE values, investigating their temporal variations and statistical trends, and finally investigating the solar spectral distributions with regards to modeling the impact of various atmospheric factors. Whereas APE is calculated from the measured spectra, simulations are carried out to generate synthetic spectra through the SMARTS model [49]. These simulations are used to analyze variations caused by parameters that lead to atmospheric extinction. The airmass and clearness index are also calculated and analyzed in order to investigate the influence of the local atmospheric conditions of each location.

2.3.1. Average photon energy

As already discussed above, APE is one of the widely used parameters that characterizes the shape of the incident irradiance spectrum [6, 18,32]. A higher blue content of the incident spectrum is correlated to a higher value of APE. Expressed in electron volts (eV), the APE is defined as [6]:

$$APE = \frac{\int_{\lambda_1}^{\lambda_2} E(\lambda)\, d\lambda}{q \int_{\lambda_1}^{\lambda_2} \phi(\lambda)\, d\lambda} \tag{1}$$

where $E(\lambda)$ is the solar irradiance at a specific wavelength λ, q is the electronic charge, ϕ is the photon flux density, and λ_1 and λ_2 are the lower and upper limits of the wavelength range under consideration. The photon flux density is given as:

$$\phi(\lambda) = \frac{E(\lambda)}{hc/\lambda} \tag{2}$$

where h is the Planck's constant, and c is the speed of light in a vacuum. Calculation of APE and integrated broadband irradiance follow the existing literature [6,14,16] and use the wavelength range (350–1050 nm) common to all spectral instruments at the five sites.

2.3.2. Atmospheric factors

In order to understand the role of various atmospheric factors on spectral distributions, the relation of these parameters with APE has been investigated. Scatter plots of APE, irradiance and solar zenith angle are created as a function of airmass. Similar plots of APE against humidity are also presented. The airmass and clearness index are calculated for each location.

Air mass

The air mass (AM) quantifies the relative increase in the pathway, and hence the amount of substance, traversed by sun rays traveling through the atmosphere compared to the shortest possible trajectory at absolute zenith (90°). In this study, AM is calculated using the sun's zenith angle from [50] as follows:

$$AM = \frac{1}{cos(\theta_z) + 0.50572 * (6.07995 + (90 - \theta_z))^{-1.6364}} \tag{3}$$

where θ_z is the solar zenith angle in degrees. The python library pvlib is used to calculate the AM values for each timestamp [51].

Clearness index

The clearness index (K_t) is a widely used parameter in categorizing the sky conditions. It is given by the ratio of total irradiance measured on a horizontal plane at the Earth's surface, to the total extraterrestrial irradiance incident on a horizontal plane at the top of the atmosphere. K_t is mathematically represented as:

$$K_t = \frac{G}{G_0} \tag{4}$$

where G is the measured horizontal irradiance, and G_0 is the calculated extraterrestrial irradiance. The sky condition is then classified using the K_t value as follows:

$$K_t = \begin{cases} clear & \text{if } K_t > 0.7 \\ partially\ clear & \text{if } K_t > 0.3\ \&\ K_t \leq 0.7 \\ cloudy & \text{if } K_t \leq 0.3 \end{cases} \quad (5)$$

The clearness index alone, however, can lead to a false classification of sky conditions because high air mass and low turbidity can produce the same clearness index as low air mass and high turbidity. Hence, in this study the spectral distributions are analyzed both in terms of variation of K_t and AM. In the same manner as for AM, the calculation of clearness index is performed using the pvlib library in python where the Spencer model is used to calculate the extraterrestrial radiation, and the solar constant is considered to be 1361 W m^{-2} [52]. The clearness index is calculated for each timestamp of the available data.

Clear-sky modeling in SMARTS

SMARTS is a FORTRAN code generally used to model the clear-sky solar spectrum by supplying atmospheric and geographic input parameters [49]. This model provides spectral irradiance in the wavelength range of (280–4000 nm) as an output. The model is based on parameterization of transmittance and absorption functions for atmospheric constituents, which include molecular (Rayleigh), ozone, water vapor, mixed gases, trace gases and aerosol transmittance. The IEC 60904-3:2019 standard prescribes using SMARTS version 2.9.2 to generate the reference spectra using the conditions displayed in Table 5 in Appendix. SMARTS is used in this work to investigate the variations in APE caused by the instantaneous conditions of five parameters, namely aerosols, airmass, altitude, ozone and water vapor. When the reference spectra are generated, the individual values of the parameters of interest are varied one by one whilst keeping the other parameters constant. The spectra generated under each of the conditions are then used to compute APE over the (350–1050 nm) range using Eq. (1).

3. Results and discussions

3.1. Distribution of APE values

APE values are calculated from the spectral irradiance datasets measured at the plane of array, within the wavelength range of 350–1050 nm, available from five different locations. The distribution of the APE values in the locations under consideration is presented in Fig. 7 as histograms. These datasets from different locations may not represent the same time period or installation angles, but all the locations contribute at least one year of data and are within the POA tilt range 30-45° with a south-facing orientation.

3.1.1. Berlin, Germany

Fig. 7(a) shows the distribution of APE values for the period of 1 year (July 01, 2020 to June 30, 2021) at Berlin, Germany. The total dataset recorded consisted of 57,143 data points; after applying the broadband irradiance filter, a total of 32,743 spectral samples remained for the analysis. The annual mean APE is found to be 1.90 eV, which indicates that the mean spectrum is blue-shifted at this location, when compared with the reference AM1.5G spectrum.

3.1.2. Enschede, Netherlands

Fig. 7(b) shows the distribution of APE values for the period of 6 years (January 8, 2014 to December 31, 2019) at Enschede, Netherlands. The total dataset recorded was 1,311,403 data points and after applying the broadband irradiance filter, a total of 783,105 spectral samples remained for the analysis. The significant drop in the number of data samples after filtering is mainly because of the data acquisition routine, which is governed by a wide time window based on the longest day of the year for that latitude (5:10 AM-10:20 PM every day). The annual mean value of APE is found to be 1.89 eV, meaning the spectrum is generally slightly blue-rich at this location.

3.1.3. Grimstad, Norway

Fig. 7(c) shows the distribution of APE values for the period of 1 year (January 1 2020 to December 31 2020) for the location of University of Agder in Grimstad, Norway. The total dataset recorded was 265,420 data points and after applying the broadband irradiance filter, a total of 203,448 spectral samples remained for the analysis. The annual mean value of APE is found to be 1.90 eV, meaning the spectrum is generally blue-shifted at this location.

3.1.4. Merklingen, Germany

Fig. 7(d) shows the distribution of APE values for the period of 7 years (January 2014 to December 2020) at Merklingen, Germany. The total dataset recorded was 1,822,200 data points and after applying the broadband irradiance filter, a total of 1,479,139 spectral samples remained for the analysis. The annual mean value of APE is found to be 1.86 eV, meaning the spectrum is generally red-shifted at this location.

3.1.5. Utrecht, Netherlands

Fig. 7(e) shows the distribution of APE values for the period of 4 years (July 19, 2014 to January 8, 2018) at Utrecht, Netherlands. The total dataset recorded was 1,147,156 and after applying the broadband irradiance filter, a total of 934,591 spectral samples remained for the analysis. The annual mean value of APE is found to be 1.88 eV, meaning the spectrum on average is similar to the reference spectrum at this location.

3.1.6. APE distribution summary

Overall, Fig. 7 presents histograms to depict the APE distribution at the five different locations. Grimstad, Norway lies at the highest latitude of 58.33°, whereas Merklingen, Germany is the lowest at 48.53°. Although these locations are characterized by the same KG climatic conditions, the local environments are quite different. Whereas Grimstad is a coastal location, the other locations are more inland with Utrecht having the shortest distance of around 60 km to the nearest sea shore.

The degree of blue shift and red shift is distinctly visible in the histograms where the difference between the mean APE and the reference APE value is highest for Grimstad, whereas the mean APE is lower than the reference APE value only at Merklingen. This indicates that, on average, spectra are shifted to longer wavelengths in Merklingen whereas spectra are shifted to shorter wavelengths for three of the other sites, i.e., Berlin, Enschede and Grimstad. Utrecht meanwhile, experiences the APE value of average spectra similar to the reference spectrum.

3.2. Clearness index variations

The monthly average clearness index for all locations is presented in Fig. 8. Measured GHI values were used to calculate K_t for all locations, except for Enschede where GHI values were taken from the NSRDB database [53]. It can be seen that Enschede and Grimstad have a higher portion of clear days in the winter months (December, January and February) compared to the other sites. For Grimstad, this represents an above average sunny winter (verified against the average of 10-year historical data at a nearby site) compared to the other datasets. Another factor to consider however, is the narrow sunshine window and subsequently lower number of data points at higher latitudes. During winter, just eliminating irradiances below 25 W m^{-2} significantly reduces the number of data points, which tends to increase the uncertainty in the results. Among the locations, Berlin is seen to have the clearest sky during summer months (June, July and August) but experiences the lowest clearness index during the winter months. Enschede and Merklingen display the least variation in clearness index conditions over the year, where the highest and lowest monthly average indexes are found to be 0.51 and 0.36 for Merklingen and 0.46 and 0.35 for Enschede, respectively.

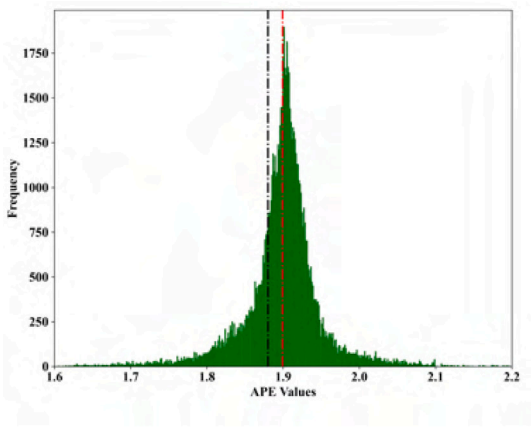

(a) Berlin (July 2020 - June 2021)

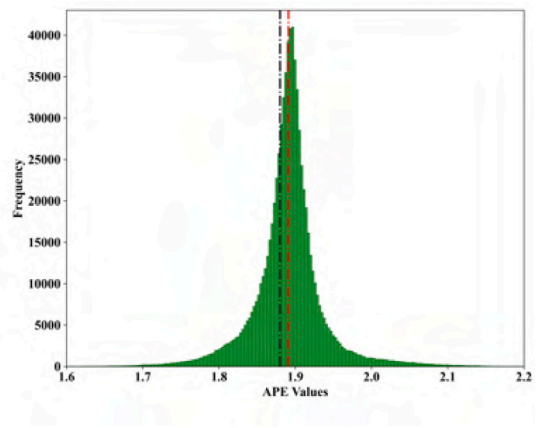

(b) Enschede (2014 to 2019)

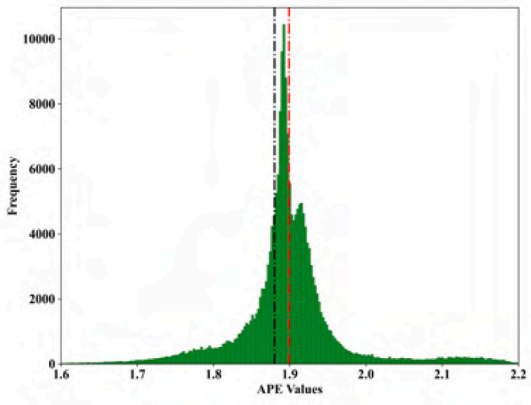

(c) Grimstad (Jan 2020 - Dec 2020)

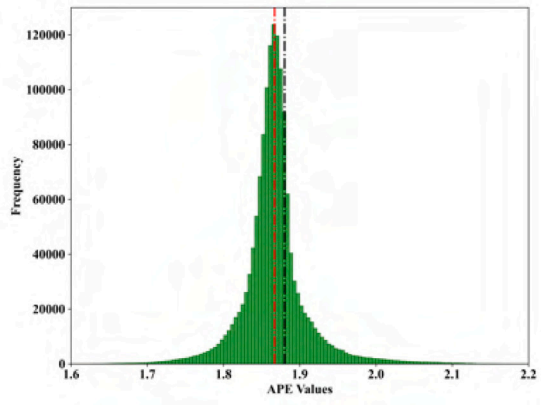

(d) Merklingen (2014 to 2020)

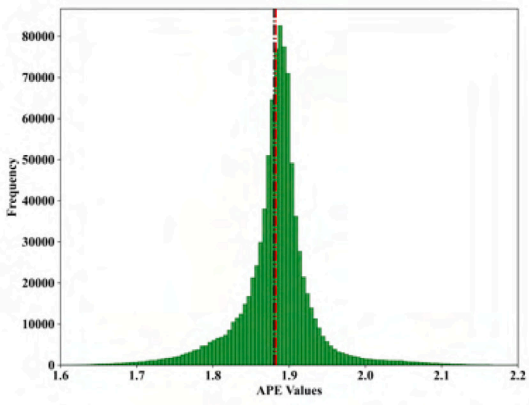

(e) Utrecht (2014 to 2017)

Fig. 7. Histograms of APE (350–1050 nm) for the five locations considered in this study, representing at least one year of APE values. The black lines indicate the APE for the reference AM1.5 spectrum while the red lines indicate the average APE in the respective locations.

The annual average APE and K_t values for each location are presented in Table 2, whereas the monthly average and standard deviation (SD) of the K_t values are presented in Table 3. The highest annual clearness index and APE values are observed for Grimstad. Merklingen records the lowest APE among the sites at 1.86 eV and K_t of 0.42, whereas Utrecht has the lowest average K_t of 0.39 and APE of 1.88 eV. As visible in Fig. 8, Berlin and Grimstad have the highest clearness index values in the summer and spring (March, April, May) months, respectively. Interestingly, both these locations experience the highest APE values during the same period.

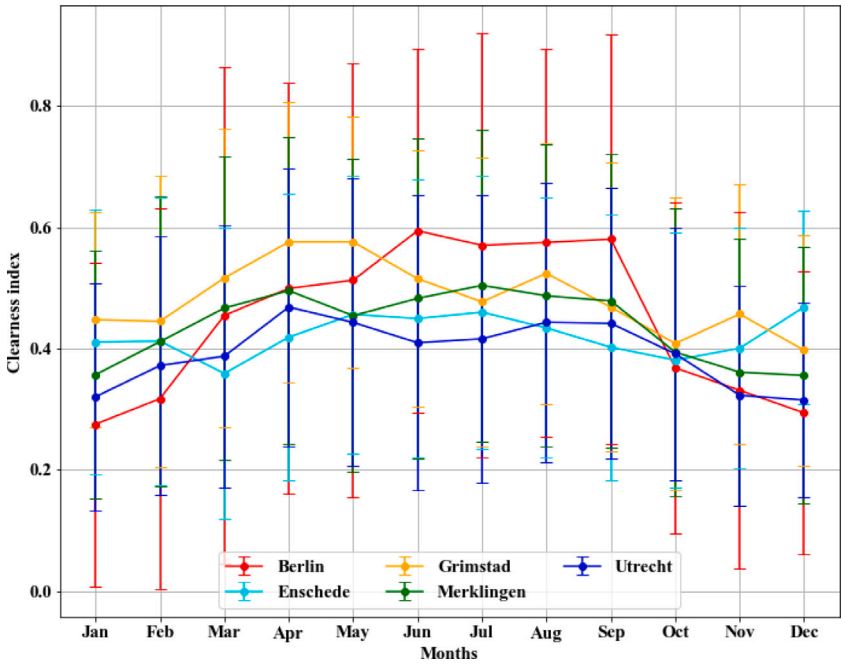

Fig. 8. Comparison of average monthly clearness index values for all locations considered in this study. The identically colored vertical lines with caps indicate the corresponding standard deviation of clearness index.

Table 2
The comparison of the annual average APE and K_t values for the five locations.

Locations	APE (eV)	K_t
Berlin	1.90	0.45
Enschede	1.89	0.42
Grimstad	1.90	0.48
Merklingen	1.86	0.44
Utrecht	1.88	0.39

3.3. Influence of atmospheric factors on APE

3.3.1. Simulation in SMARTS

As spectral irradiance is dependent on various atmospheric factors and all the participating institutions had different conditions under the measurement periods, it is important to first investigate the parameters that introduce considerable variations in the spectral distributions. A general simulation of spectra in SMARTS has been undertaken to investigate the variation of spectral irradiance caused by multiple factors. The simulations are conducted on two fronts, considering the global variations of the factors, and the local variations typically reported in the northern European locations. The impact of the atmospheric constituents and factors, namely, aerosol optical depth (AOD), precipitable water vapor (PWV), ozone, airmass and altitude on clear sky irradiance were investigated using prescribed values in SMARTS 2.9.2. The reference spectrum was generated as per IEC 60904:3-2019 and the respective values for the above mentioned atmospheric factors were varied from the reference spectrum, one by one whilst keeping the other parameters constant, to generate the synthetic spectra. APE was then calculated for each spectra and the individual cases presented as a radar plot can be seen in Fig. 9.

Relevant information regarding the atmospheric factors and their respective values used to create the radar plot is provided in Table 4. Fig. 9 shows that AM and PWV cause the greatest variations in spectral irradiance, both globally and in northern Europe. AOD is seen to induce lesser variations in spectral irradiance in northern Europe compared to across the globe. Altitude and ozone have the least impact among atmospheric parameters studied on both conditions.

The APE values resulting from modeling with the different set of input parameters show that aerosols are an important atmospheric constituent which affect the spectral distribution. Aerosols influence global climatic conditions [54] with various thermal, direct and indirect effects on the atmosphere [55]. The major atmospheric extinction effect of aerosols is scattering (with a strong forward scattering component), whereas some aerosols also absorb the incident radiation [1], thus altering the radiative balance of the atmospheric system. To understand the impact of AOD, the values at 500 nm wavelength are varied in increments between 0.01 to 1.0 so as to simulate the variation from pristine to extremely polluted locations. Rather than dust, northern Europe is frequently impacted by smoke and pollution episodes and the AOD range of 0.01 to 0.3 is reported for this region [56,57]. For the global variation of AOD, the resulting APE values are seen to reduce from 1.89 eV to 1.86 eV. This is accompanied by the reduction of integrated broadband irradiance in the 350–1050 nm wavelength range from 784 W m^{-2} to 598 W m^{-2}. Similarly, for northern Europe, increasing AOD values from 0.01 to 0.3 is found to reduce the integrated broadband irradiance in the same range from 784 W m^{-2} to 723 W m^{-2} whereas the APE reduces from 1.89 eV to 1.88 eV. These results indicate that the higher AOD values cause the reduction in broadband irradiance and subsequently the APE values, with a red-shift of the incident spectrum. Due to the generally lower values of aerosol loading across northern Europe, the impact of AOD on the spectral distributions is less pronounced compared to other regions that experience higher AOD levels [58,59].

Simulations show that precipitable water vapor is another major parameter affecting the atmospheric extinction. PWV is mostly concentrated in the boundary layer, up to 2–3 km above the surface [1], and is dependent on the location and time. The PWV values are varied from 0 cm to 10 cm as global minima and maxima, based on the fact that PWV can reach up to around 10 cm over very hot/humid tropical areas [60]. This results in a blue-shift for APE from 1.85 eV at 0 cm to 1.93 eV at 10 cm water column. The integrated broadband irradiance in the (350–1050 nm) wavelength range reduces from 801 W m^{-2} to 709 W m^{-2} with respect to the increased water vapor content. However, in northern Europe the highest PWV content observed is around 3–3.2 cm during the July–August months [61,62]. When simulated in this range, the same integrated broadband irradiance is seen to drop

Table 3
Monthly average and standard deviation of clearness index for all locations.

Months	Berlin		Enschede		Grimstad		Merklingen		Utrecht	
	Mean	SD	Mean	SD	Mean	SD	Mean	SD	Mean	SD
Jan	0.276	0.267	0.411	0.218	0.448	0.178	0.357	0.204	0.320	0.187
Feb	0.318	0.314	0.412	0.237	0.445	0.239	0.411	0.239	0.372	0.213
March	0.455	0.410	0.359	0.241	0.516	0.246	0.467	0.251	0.388	0.217
Apr	0.499	0.339	0.419	0.236	0.576	0.231	0.495	0.254	0.468	0.229
May	0.513	0.357	0.456	0.230	0.576	0.207	0.454	0.258	0.443	0.237
Jun	0.594	0.300	0.449	0.229	0.515	0.211	0.483	0.263	0.410	0.243
Jul	0.570	0.349	0.460	0.226	0.477	0.238	0.504	0.257	0.416	0.237
Aug	0.575	0.320	0.434	0.214	0.524	0.215	0.487	0.249	0.443	0.230
Sep	0.580	0.337	0.402	0.219	0.468	0.239	0.479	0.242	0.442	0.223
Oct	0.368	0.272	0.381	0.210	0.408	0.241	0.394	0.236	0.391	0.208
Nov	0.331	0.294	0.400	0.198	0.457	0.213	0.361	0.220	0.323	0.181
Dec	0.294	0.233	0.468	0.159	0.397	0.191	0.356	0.211	0.315	0.160

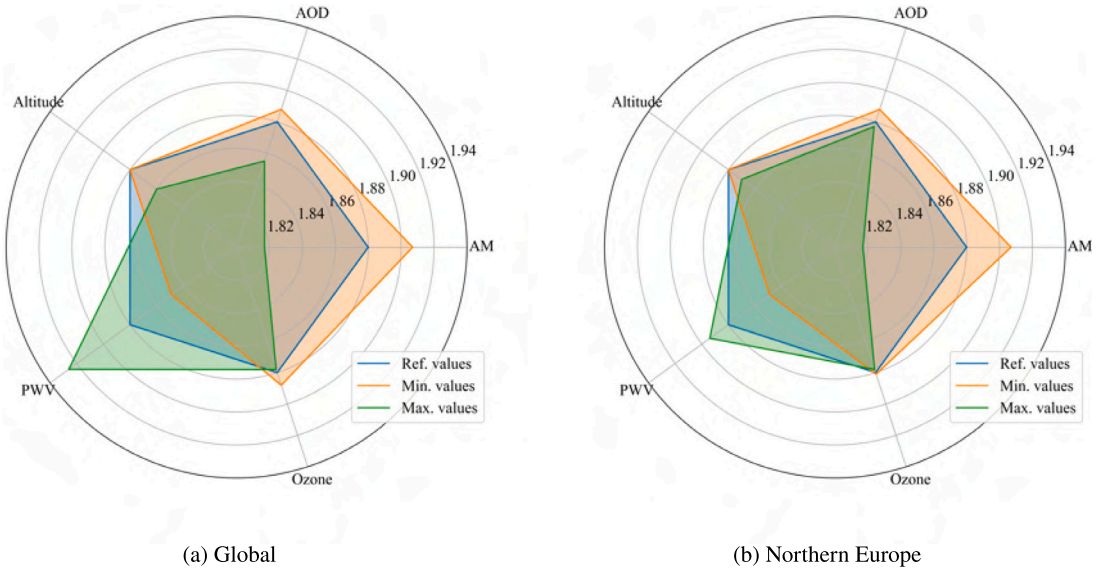

Fig. 9. Radar plot of the APE calculated for reference, minimum and maximum values of each atmospheric factor contributing to the simulated spectra in SMARTS for global and northern European locations. The values used to generate the spectra resulting these APE values are presented in Table 4.

Table 4
Values used for the variation of atmospheric factors shown in the radar plot.

Parameters	Global			Northern Europe	
	Ref value	Min value	Max value	Min value	Max value
Air mass	1.5	1	4	1	4
AOD	0.084	0.01	1	0.01	0.3
Ozone (atm-cm)	0.34	0.1	0.5	0.2	0.5
Altitude (km)	0	0	5	0	3
PWV (cm)	1.42	0	10	0	3.2

from 801 W m^{-2} to 743 W m^{-2}, while the APE values increase from 1.85 eV to 1.89 eV. Although the drop in broadband irradiance is seen, the wavelengths in the visible range of spectra are less affected by the water vapor compared to the infrared range, as most of the absorption by water vapor is at longer wavelengths [1]. Therefore the APE values are generally found to be higher during elevated water vapor content in the atmosphere, causing the spectrum to subsequently shift towards the blue region.

Ozone is normally present in the stratosphere of the Earth's atmosphere and is known to absorb in the ultraviolet (UV) and blue region of the visible range of solar radiation. The ozone concentration in the atmosphere is constantly changing with the seasonal patterns and solar intensity. Ozone is produced mostly over the tropical region and is transported to the poles by winds. Globally, for the variation of ozone from 0.1 atm-cm to 0.5 atm-cm [63], the APE value reduces from 1.89 eV to 1.88 eV with the integrated broadband irradiance dropping from 776 W m^{-2} to 757 W m^{-2}. Moreover, the ozone concentration in northern Europe can vary from 0.2 atm-cm to 0.5 atm-cm [64] and the subsequent APE values are seen to remain around 1.88 eV, only reducing in terms of the third order of decimals. During the same variation of ozone, the integrated broadband irradiance over 350–1050 nm wavelength range is observed to reduce from 770 W m^{-2} to 757 W m^{-2}. The absorption caused by enhanced ozone content only contributes to a ever so slight increment in the red-richness of the spectra.

Increasing altitude leads to significantly increased broadband surface irradiance [65,66]. The results from the simulation show that the APE values decreased from 1.88 eV at the sea level to 1.87 eV at the altitude of 2.5 km and to 1.86 eV at 5 km above sea level. The results are in good agreement with a similar study conducted by [66], where the irradiance was seen to increase at all wavelength regions with the increment in altitude, but the increment in the power density of photons in the IR region was found to be around 27%, while it was observed to be 20% for UV and 6% for the visible region. Since the 350–1050 nm wavelength range used in this study leaves out UV-B and UV-C ranges in APE calculations, the overall gain on power density at UV regions is reduced and thus the overall spectra become red-shifted.

Air mass is also a major parameter that influences the spectral variation, where the APE values are seen to shift from 1.91 eV to 1.82 eV as the air mass varies from AM1 to AM4, the latter corresponding to a solar elevation angle of around 15°. The selection of

AM4 as a threshold for the simulations is determined by balancing the appearance of the radar plot with a sufficiently large range of solar elevation for evaluation purposes. To illustrate, if the APE at AM5 is 1.76 eV and incorporated into the radar plot, it would visually obscure the effects of other factors. With increasing AM, irradiance shifts toward longer wavelengths because more of the short wavelength radiation is attenuated due to Rayleigh scattering [67]. Higher values of AM values will obviously occur at all locations depending on the time of day and year. As a result, even greater degrees of attenuation can be anticipated.

3.3.2. Impact of GPOA irradiance on APE

The relation between broadband GPOA irradiance and APE is presented in Fig. 10, where the color-bar represents the corresponding AM values. The figure includes the histogram distribution of the values along both axes for each location. As seen from the figure, the irradiance values in three locations range up to 1400 W m^{-2}, except for Berlin and Enschede where the irradiance values are seen to reach up to 1200 W m^{-2}. The AM values range from 1 to over 35 in four locations except for Merklingen where the AM values reach up to around 28. As visible in the figure, the APE values have a wider spread in the lower irradiance conditions and with the rising irradiance values, the APE spread gradually narrows. When the highest irradiance conditions are achieved the APE values are grouped around the reference APE value of 1.88 eV. High broadband irradiance conditions are mostly characterized by a solar position closer to the zenith, i.e., low AM conditions. These conditions indicate a low atmospheric extinction and thus spectra closely matching the reference AM 1.5G spectrum. The monthly distribution of the clearness index has been already presented in Fig. 8 and it is seen that the summer months have naturally higher values compared to the winter months. Higher clearness index values in spring and summer months stem from the lower degree of cloud cover. During these periods with the high irradiance and low AM, the higher energy share in the blue part of the spectrum contributes to the higher APE values, also visible in the figure. But during similar irradiance conditions when AM gradually gets higher, the atmospheric extinction increases and subsequently the APE values fall below the reference value. High irradiance values normally result from the high DNI values for clear sky conditions. As diffuse spectra do not shift a lot with AM [68], a shift in DNI spectra governs the resulting APE value. Spectra measured at high AM are seen to produce low APE values in all locations. Under specific conditions, very high APE values occur at low irradiance and low AM, manifested by a high share of diffuse irradiance where wavelength ranges in the infrared part of the spectrum are absorbed by water molecules in the clouds, as well as when the solar position is behind the plane of the spectroradiometer such as for tilted planes at high latitude locations, e.g. [69]. Very low APE values occur at low irradiance and high AM, characterized by clear sky conditions and low solar elevation during the early mornings or late evenings.

3.3.3. Impact of solar zenith angle on APE

The relation between solar zenith angle and APE is presented in Fig. 11, where the color-bar represents the corresponding AM values. The figure includes the histogram distribution of the values along both axes for each location. A clear dependence of the APE values to zenith angle is visible. As previously presented in Eq. (3), AM and zenith angle are directly related. Therefore, in this section, AM and zenith angle can be considered as representing the same condition. The color-coded AM values are used to facilitate a better understanding of the APE distribution with respect to solar elevation. The zenith angle for three locations, namely Berlin, Enschede and Utrecht are similarly distributed between 30° to 90°, due to these locations lying in the same latitude. For Grimstad, the zenith angle varies from around 35 ° to 90°, while for Merklingen the zenith angle ranges from 25° to 90°. When zenith angle and AM reach their lowest values around noon, on a clear sky day irradiance is also at its peak, barring over-irradiance conditions [70,71]. As visible from Fig. 11, a distinct ‘funnel’ shape appears for all the locations where APE values during low AM (low zenith angle) are less dispersed compared to periods with large solar zenith angles when the sun is close to the horizon. The natural range of variation of atmospheric parameters and the attenuation caused by them is constrained due to the shorter path length compared to high AM conditions. Conversely, the high variance of atmospheric parameters during high AM conditions gives rise to a larger variation of APE values.

Comparing the locations, a significantly smaller dispersion of APE values is observed for Berlin and Grimstad during periods with low AM values. Such narrow dispersion of APE values can be correlated to the site specific conditions as both of these locations are characterized by highest clearness index values and also highest APE values during the spring and summer months. Among other factors, this could also be related to the number of data-points available as the other sites possess at least four years of data, compared to a single year of data for Berlin and Grimstad.

3.3.4. Impact of humidity on APE

As the precipitable water vapor measurements were not available in all of the participating sites, humidity is used instead as the parameter to quantify the presence of water vapor in the atmosphere, mainly because the humidity and PWV have a linear relationship [72]. The relation between humidity and the APE could not be established with the complete dataset. However, when the APE values are filtered for a clearness index higher than 0.7, i.e. clear sky conditions, the potential relation between APE and humidity is established and the scatter plots are presented in Fig. 12. The plots are indexed by ambient temperature for the respective locations. Also, the analysis for Enschede is not included in this section due to the unavailability of the required data. The humidity in Berlin and Grimstad ranged between 25% and 90%, whereas for Merklingen and Utrecht it ranged from around 20% to 100%. The average humidity for the clear sky conditions ranged from 40%–50% in Berlin and Grimstad to around 50%–60% in Merklingen and Utrecht. The temperature distribution is fairly similar in all locations, with the maximum temperature of slightly above 30 °C seen for three locations while only Berlin experienced the highest temperature above 35 °C. The minimum temperatures for most locations were recorded to be between 0 °C and −10 °C, with only Merklingen observing the temperatures below −10 °C with lowest temperatures reaching around −15 °C.

For periods with low humidity and high temperatures, the APE values are seen to generally lie closer to the reference APE value. Lower humidity levels imply lower atmospheric extinction enforced by the water vapor while the higher temperatures suggest the periods of the day with higher solar elevation, i.e. low airmass. Also, the higher temperatures during the clear sky conditions indicate the summer months in the northern hemisphere, where the APE values are generally higher due to high energy content in the blue part of the spectrum. As seen in Fig. 9, AM and water vapor are the two major parameters producing variations in APE both globally and in northern Europe. Low water vapor concentrations (lower humidity) and low AM values (achieved during higher temperatures) represent the generally narrow dispersion of APE value close to the reference value of 1.88 eV, in three locations except for Berlin. The dispersion of APE values gradually widen with the increment in humidity for Merklingen and Utrecht whereas it remained constant for both Berlin and Grimstad.

Interestingly, the instances with high humidity and low atmospheric temperature are seen to yield low APE values in all four locations. The clear sky conditions with low temperatures and high humidity indicate the winter periods in the northern hemisphere where airmass is higher. These conditions mean that the spectrum is generally shifted to the longer wavelength regions despite higher water vapor content in the atmosphere. The atmospheric extinction in the blue-rich region of the spectrum is also enforced by the higher concentration of ozone molecules in the mid and high latitude conditions [73]. Although ozone showed little impact on the APE values in the SMARTS simulation, it can contribute to the extinction in the UV and visible blue ranges together with the other atmospheric and environmental factors.

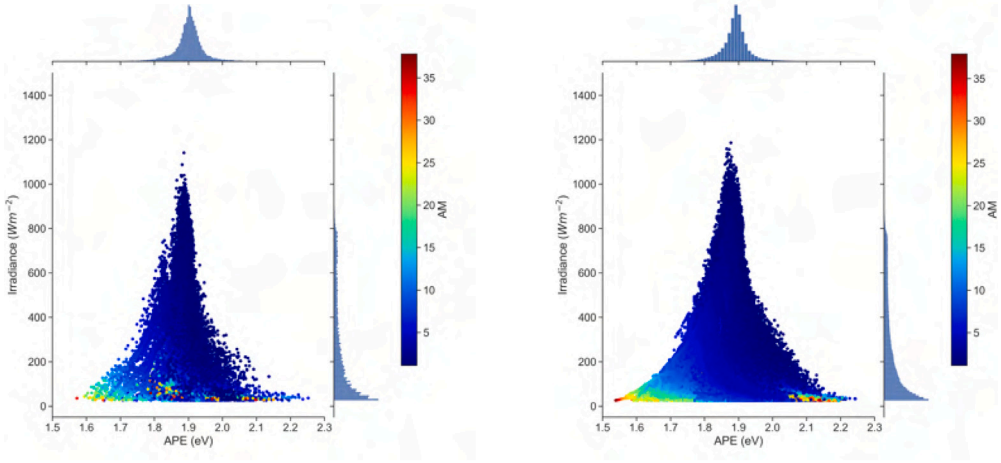

(a) Berlin (b) Enschede

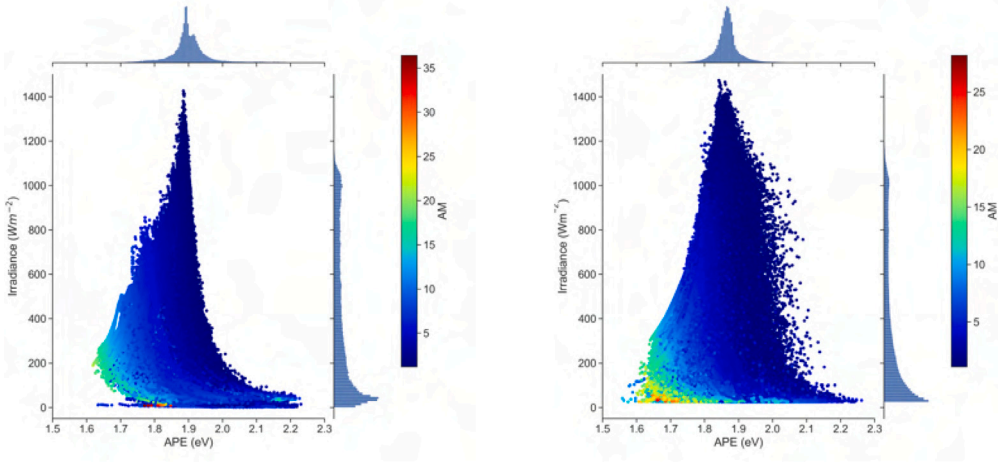

(c) Grimstad (d) Merklingen

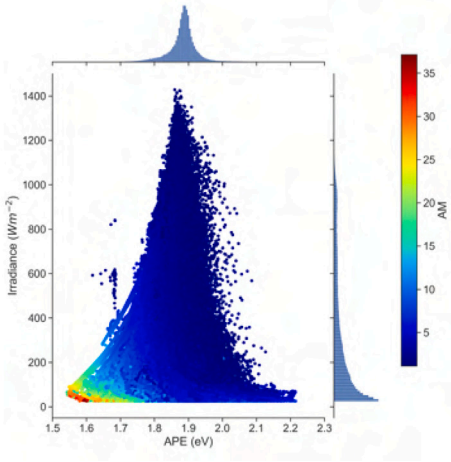

(e) Utrecht

Fig. 10. APE against the broadband irradiance (GTI) for the experimental locations. The histogram distributions of the values along both axes are also presented. The color-bar represents the AM values.

3.4. Monthly distribution of APE values

The monthly distribution of APE values in the five locations is compared for clearness index ranges as proxies for sky conditions at each location, for the months of June and December. These months represent the distributions of comparatively higher and lower APE values at each site. June is chosen as a representative month where the clearness index is relatively high for all locations. Using the same logic for winter, the month of December is chosen where K_t is relatively lower in all locations. For the month of June, a single peak histogram of APE values is seen in all four locations except Grimstad as shown in Fig. 13 where the contributions of cloudy sky and partly clear to clear conditions are separately presented. Cloudy sky conditions in Grimstad contribute to a narrow APE distribution with modal value

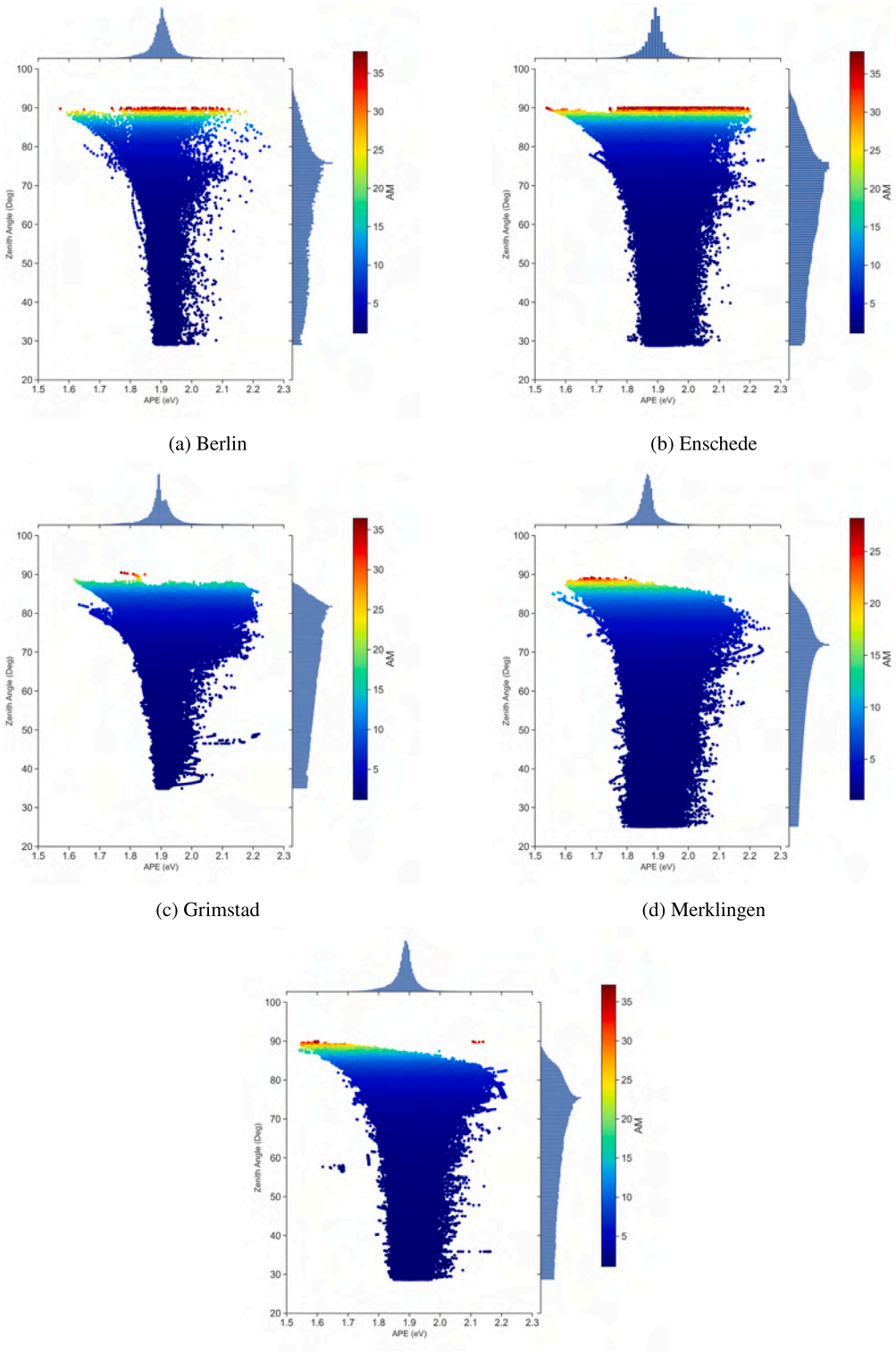

Fig. 11. APE against the solar zenith angle for the experimental locations. The histogram distributions of the values along both axes are also presented. The color-bar represents the AM values.

around 1.92 eV, whereas combined clear and partly clear conditions give rise to modal value of APE distributions around 1.89 eV, resulting to a bi-modal peak in the histogram.

For the month of December, the histograms for all five sites in Fig. 14 show a distinct bi-modal distribution where the contribution of cloudy sky conditions is clearly evident. The average APE values for the combined clear and partially clear sky conditions have a significant difference across locations, where the average APE at Enschede, Merklingen and Utrecht lies around 1.78 eV, while the mean APE at Grimstad and Berlin is 1.74 eV and 1.82 eV respectively. Meanwhile for cloudy conditions, the average APE of all locations lie between 1.87 eV and 1.90 eV. As also exhibited by the radar plot in Fig. 9,

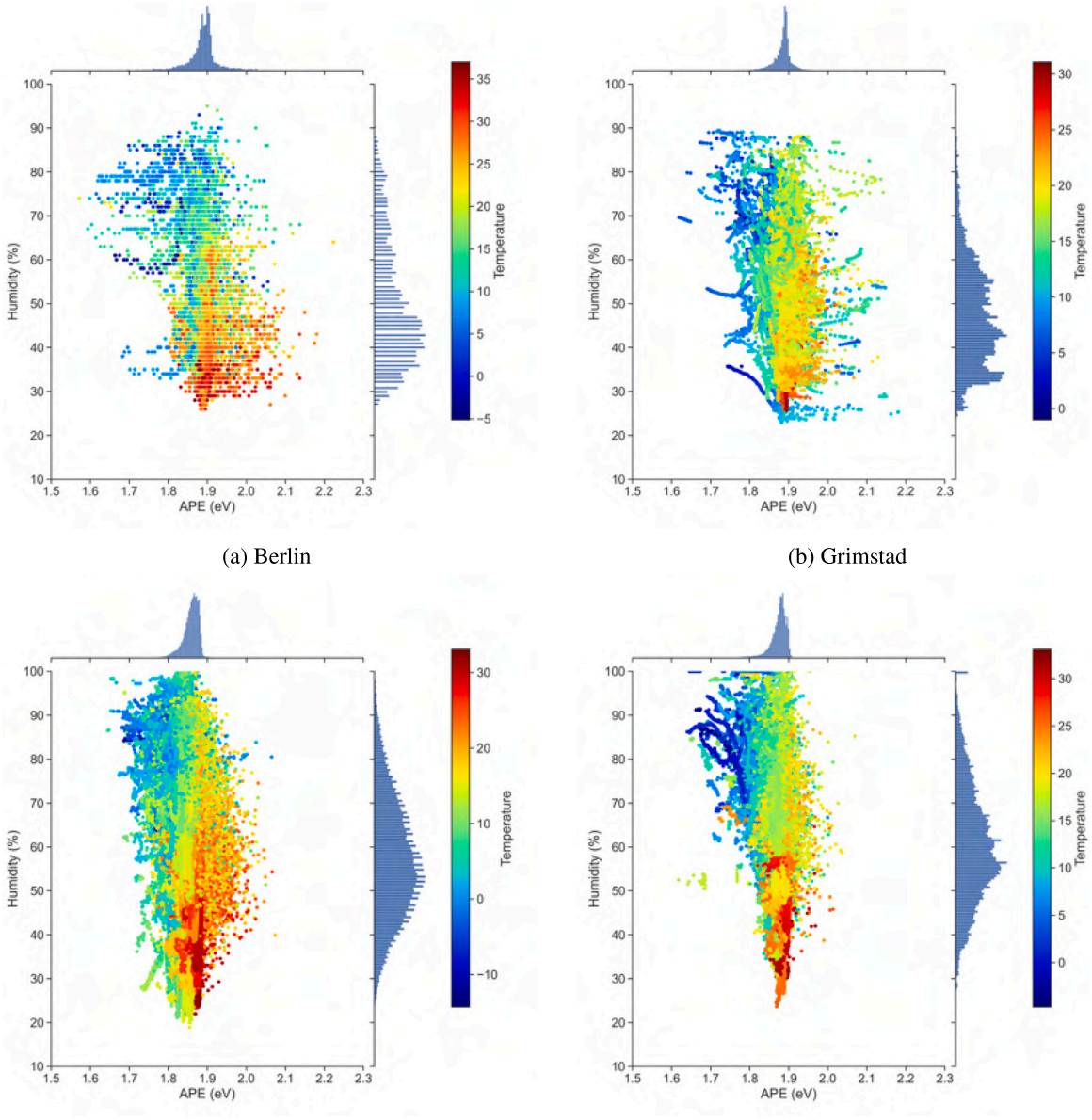

Fig. 12. APE against the humidity for $K_t > 0.7$ for the experimental locations. The histogram distributions of the values along both axes are also presented. The color-bar represents the AM values.

the generally prevalent higher AM conditions and absorption of long-wave low energy spectrum by water vapor during clear sky conditions in winter cause the average APE to remain significantly below the reference value of 1.88 eV. The variations in APE across the five locations in these periods however arise from the difference in local conditions.

3.5. Inter-comparison of results from different locations

The monthly average APE for all locations is presented in Fig. 15. Overall, all five locations show higher average APE values during the summer and lower averages during the winter months. In general, a higher share of clear sky conditions during the summer months in each location with higher energy content in the blue-rich region of the spectrum yields higher APE values. The relation between APE and K_t depends on the time of the year, as reported by [74]. The lower AM values in the summer months for the northern hemisphere cause more blue-rich spectra, giving rise to higher APE values. Similarly, cloud covers shift the spectrum to the blue region mainly due to higher absorption in the infrared caused by water vapor [74]. These factors cause the average value of APE to remain higher during the summer. Although cloudy sky conditions similarly would yield higher APE values in winter, the effect is counteracted by high AM values and the occurrence of occasional clear sky conditions that result in the average APE values remaining lower.

The APE values for Grimstad undergo the highest variations compared to the other locations, whereas lowest variations are visible in Merklingen. As seen earlier from the monthly distribution of the clearness index (Fig. 8), Grimstad has the highest K_t among the analyzed locations, and with the high latitude and high relative AM, this results in a significant red shift of the spectrum during the winter periods with

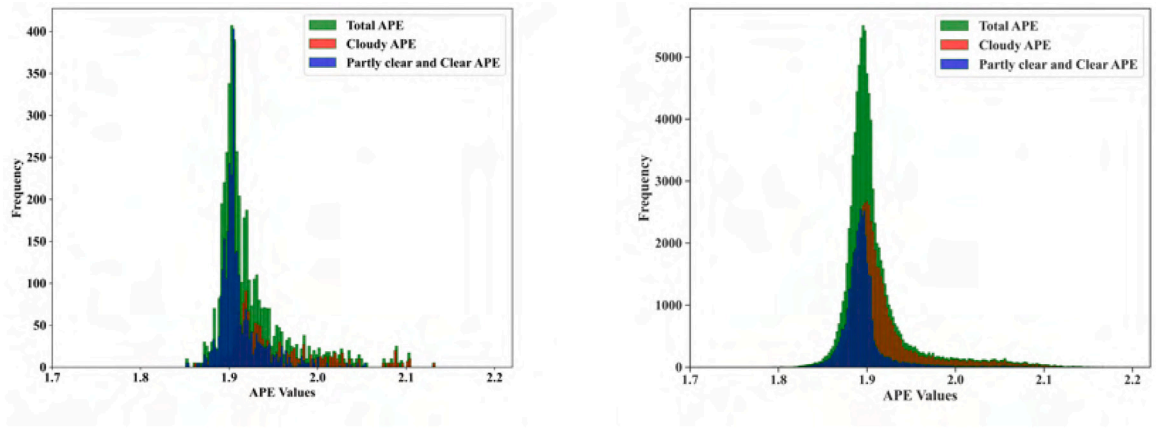

(a) Berlin

(b) Enschede

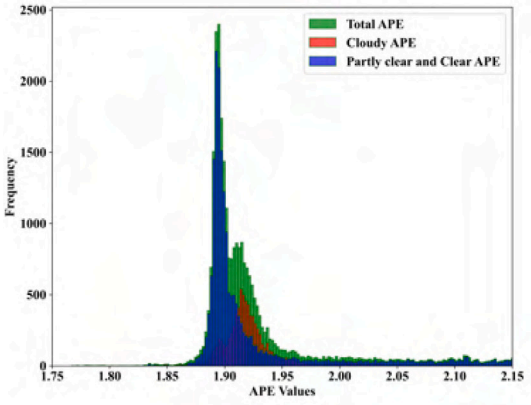

(c) Grimstad

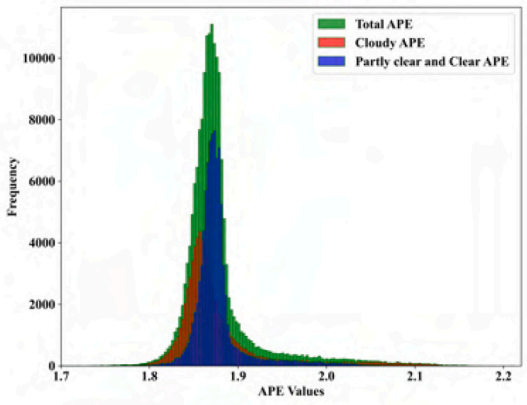

(d) Merklingen

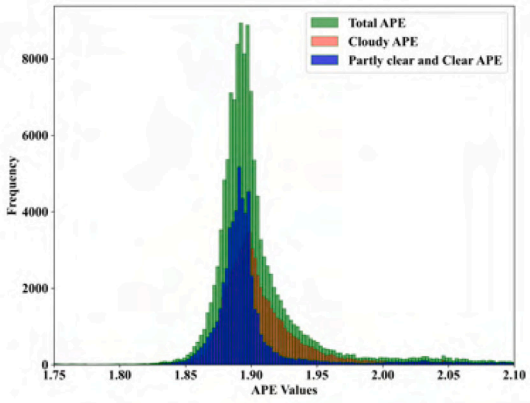

(e) Utrecht

Fig. 13. APE histogram for the month of June. Contribution of cloudy sky conditions is additionally presented within the histogram based on K_t cases as presented in Eq. (5).

mean APE values around 1.82 eV. Grimstad experiences the highest and lowest monthly APE values among five locations, from 1.93 eV in July to 1.82 eV during December and January. The APE values for Merklingen are 1.88 eV in July and 1.84 eV in December. APE values for Berlin ranged from 1.86 eV in December to 1.92 eV in June, APE values for Enschede ranged from 1.85 eV in December to 1.91 eV in July, and APE values for Utrecht ranged from 1.84 eV in December to 1.91 eV in July.

Results show that all of the locations except Berlin encounter higher APE values in the month of July, while all experience the lowest APE value in December. Fig. 15 points to the latitudinal dependence of APE values, which was also tested in SMARTS. The sheer impact of latitude was however not found to significantly affect the APE in the SMARTS simulations. The AM and the micro-climatic conditions, with factors such as aerosols, PWV and others being important contributors, therefore determine the APE values.

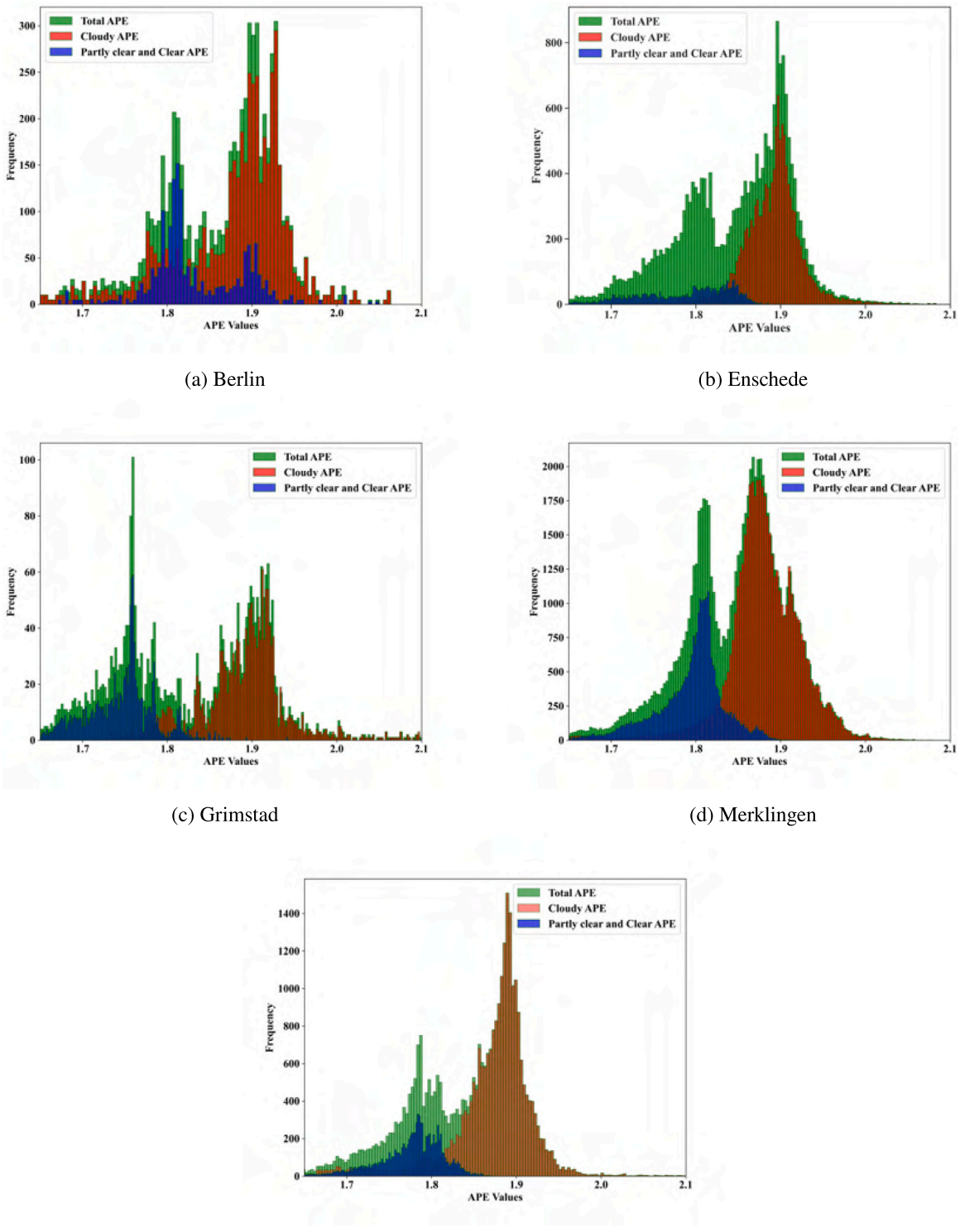

(a) Berlin

(b) Enschede

(c) Grimstad

(d) Merklingen

(e) Utrecht

Fig. 14. APE histogram for the month of December. Contribution of cloudy sky conditions is additionally presented within the histogram based on K_t cases as presented in Eq. (5).

In addition to the general distribution of APE values in each location, a comparison of the raw spectra from each location during noon of a clear day in summer and winter, normalized to the maximum spectral irradiance intensity value, is also presented in Fig. 16. Due to the difference in resolution between instruments, the spectral irradiance data from SolarSIM-G is smoothed using a 5 nm central averaging technique, to better match the lower spectral resolution of the spectroradiometers as in [42] for the similar instruments. As seen from Fig. 16(a), a similar qualitative shape of the spectrum is observed for all locations during the summer. In comparison, the spectrum recorded during the winter represents higher variation in the spectral irradiance intensity at various wavelengths resulting in a significant variation among the APE as presented in Fig. 16(b). While spectral irradiance intensity at Grimstad is higher at NIR regions for both winter and summer months, the intensity at UV and visible range during winter months is significantly lower than other locations. In summer months, the energy

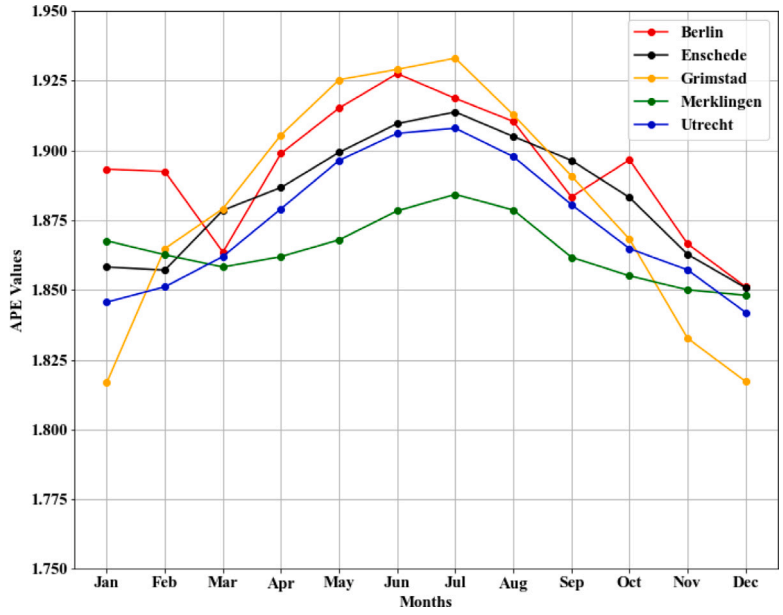

Fig. 15. Comparison of monthly average APE values for the various locations considered in this study.

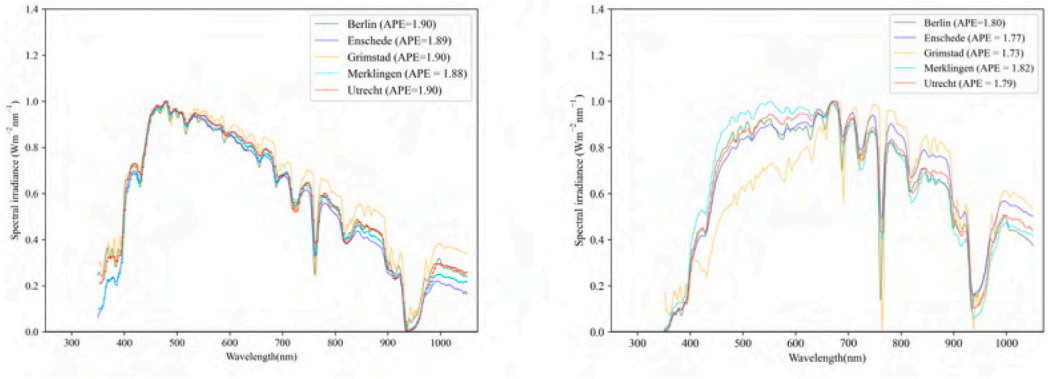

(a) Summer (b) Winter

Fig. 16. Normalized measured spectra from around noon of a clear day in summer and winter months at each location.

distribution in UV and visible region is quite similar across all locations and significant difference is observed at NIR regions only. Merklingen experiences higher spectral intensity in the wavelength ranges below 700 nm while Grimstad experiences the lowest amongst all locations which correlates to the APE value of 1.82 eV in Merklingen and 1.73 eV for Grimstad. Berlin, Enschede and Utrecht experience similar spectral distributions across all wavelengths, with spectra at Enschede having lower energy content up to visible range and higher in the infrared range among locations lying on the similar latitude. The APE values for the spectra during winter months are distributed similar to the monthly average APE values of corresponding locations.

Moreover, the spectra resulting to the same APE values are also compared from each locations and presented in Fig. 17. The comparison involves the calculated average spectrum from spectra measured over an hour from all locations, which is normalized to the maximum spectral irradiance intensity value. These spectra are selected from two periods, summertime (May–June) for APE 1.88 eV and wintertime (November–December) for APE 1.82 eV. These spectra result from different days of the year for each location. For the normalized spectra resulting in APE of 1.88 eV, all locations experienced highest energy content between 450–500 nm. The average spectra from Grimstad is seen to have relatively higher energy content in both the UV and IR regions compared to other locations, while having lower energy content in the visible region. However, for the normalized spectra yielding APE of 1.82 eV, both Utrecht and Merklingen experienced higher energy content around 550 nm whereas for other locations, the highest energy content was at around 675 nm. Similar to the average spectra for the APE of 1.88 eV, the energy content in Grimstad was observed to be higher at UV and IR regions. Among other reasons, the difference in spectra seen between Grimstad and other locations could also be influenced by the instrumentation, as all other locations except Grimstad use a array type spectroradiometer, and from the same manufacturer.

Although the spectra correspond to the same APE value, it should be noted that the AM conditions and the integrated irradiance were different for all locations. It is known that the same integrated irradiance can result from different spectra [75] whereas different spectra can yield same APE value [22,23,31]. As demonstrated in the radar plot in Fig. 9, APE has a strong dependence on aerosols, airmass and water vapor. The different combination of these constituents cause atmospheric extinction of different magnitudes which can at times yield the same APE values for different spectra, which has also been highlighted by [31].

In addition to the dynamic factors discussed above, the site conditions like POA tilt and spectral albedo can also significantly alter the measured spectra. While the ground reflected radiation can amount to

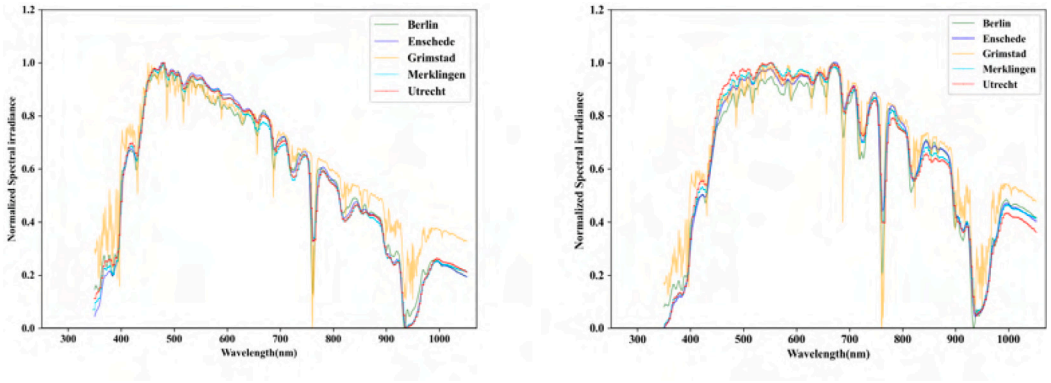

Fig. 17. Average measured spectra around noon of different clear days in (a) summer and (b) winter, yielding same APE values at each location.

less than 1% of the total irradiance for tilt angles less than 25° [76], this can considerably rise with the increment in the tilt angle. To assess the impact of tilt angle and albedo types on APE, SMARTS simulations similar to Section 3.3.1 were performed on the reference spectrum with four different albedo types (alpine meadow, concrete, fresh snow and light sand) where the tilt angles were varied between 0° and 50°. As presented in Fig. 18, the albedo from fresh snow consistently contributes to higher APE for all tilt angles, followed by concrete, light soil and alpine meadow. As the tilt angle gradually increases from 0° to 50°, it is seen that the APE values consistently decrease for all the albedo types, and the corresponding integrated irradiances in the 350–1050 nm wavelength range increase. Difference in zonal (far-field) albedo causes the irradiance and subsequently the APE to vary even when the receiver is at a 0° tilt, but the same would not be true for differing near-field albedo with a same zonal albedo [77]. In the same figure, APE values contributed by different spectral albedos between 30°– 45° tilt angle are marked within a gray rectangle to represent the locations considered in this study. This difference in APE values from each albedo source is quite small, i.e., in the order of less than 0.01 eV, which is rather an insignificant difference. Similarly, the difference in APE for the tilt angle range is relatively similar for all four albedo cases, meaning the uncertainty caused by differing tilt factor alone is small, provided the albedo is similar for the different locations. However, the difference is significant in case of highly reflective albedo source like snow, compared to the low albedo ground covers. For example, for a 30°–45° tilt angle range, the maximum difference of APE between a high and low reflective ground cover would be in the order of 0.03 eV, which is comparable to the shifts among locations in this study. Spectral albedo, therefore is an important factor that causes differences in results that are not related to the atmosphere/solar radiation itself, but rather the local environment. In addition, Moreover, dissimilarity in instrumentation specifications can also introduce variations in the recorded spectrum and hence, in the APE. Due to the scope of the paper, characteristics of the spectral albedo is not investigated in this paper but is suggested as a topic for future work.

Although the raw spectra differ amongst locations, the shape of the normalized spectra is observed to be qualitatively similar for a given APE value. A general shift of the spectra to the blue rich region in the reported locations indicate possibilities of overall spectral gain for PV devices with narrow SR both in single and multi-junction cells. However, it should be noted that these locations experience red rich spectra during clear days in wintertime and thus PV devices with wider SR can experience spectral gain in winter.

4. Conclusions

The spectral irradiance distribution from five different locations in northern Europe is compared on the basis of APE as a parameter of spectral variation. The results show that the annual average spectra in these locations, except for Merklingen are shifted to the blue-rich region compared to the reference AM1.5G spectra. Clearness index was used to investigate the sky conditions in these locations and results validated the prevalence of generally blue rich spectra contributed by a higher share of diffuse irradiance conditions. The clearness index results show that monthly average values of K_t mostly lie under 0.5, with some exceptions for Berlin and Grimstad. The annual average APE of 1.90 eV, 1.89 eV, 1.90 eV, 1.86 eV, and 1.88 eV was calculated for Berlin, Enschede, Grimstad, Merklingen, and Utrecht respectively.

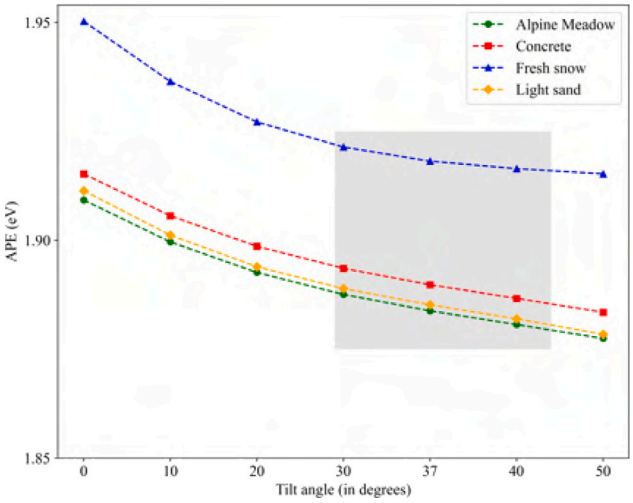

Fig. 18. Contribution of different albedo types at various tilt angles on the APE; simulated based on the reference AM1.5 spectrum in SMARTS.

The seasonal variation of APE appears to increase with latitude, with the highest seasonal variation in Grimstad (1.82 eV in winter and 1.93 eV in summer) and lowest seasonal variation observed in Merklingen (1.85 eV in winter and 1.88 eV in summer), i.e., the highest and lowest latitude locations considered in this study. The comparison of spectral distributions in summer and winter months show a bi-modal distribution of APE values during winter, where clear contributions from clear and cloudy sky conditions can be distinguished for all locations. Simulations in SMARTS indicate that the observed latitude-dependent variation is actually caused by the location-specific range of AM values and atmospheric parameters. It is evident from the simulations that the spectral distributions are primarily influenced by two atmospheric parameters, namely AM and PWV, for the northern European conditions while aerosols seem to have an additional impact on a global level.

The relationships between APE and air mass through zenith angle, irradiance and humidity are also explored. For low zenith angles, i.e. low AM values, the results show a wider distribution of APE values for Merklingen and Utrecht, compared with Grimstad and Berlin where APE values are narrowly distributed around 1.91 eV for zenith angles below 35°, probably because both Berlin and Grimstad are characterized by the higher clearness index values and also the highest APE values during spring and summer. Similarly, a wider distribution of APE values during low irradiance conditions is encountered which correlates to the higher AM values. The extreme APE values found in these locations are contributed by the irradiance conditions during early mornings and late evenings as well as extremely cloudy conditions. Low solar elevation angles shift the APE values towards the red region and values as low as 1.6 eV are observed. During cloudy conditions, when the long-wave radiation is absorbed by water molecules in the clouds and the spectrum shifts to the blue region with APE values up to 2.2 eV. APE values during high irradiance conditions are typically centered around the reference APE value of 1.88 eV. The impact of humidity on APE values is visible after filtering the datasets for $K_t > 0.7$, where for high temperature and low humidity conditions, the APE values are gathered near the reference value. Lower temperature conditions representative of winter periods with higher AM values experience APE values as low as 1.7 eV, even during high humidity conditions.

The results presented here for the spectral distributions of GPOA irradiance for five locations in northern Europe add to the existing limited knowledge on spectral variations at different geographical locations. As this work demonstrates, the spectral distributions are subject to micro-climatic conditions and although the locations are within the same climate classification they have significant differences in their monthly and annual average APE distributions. These differences arise mainly due to solar elevation combined with atmospheric factors, although some contribution is attributed to the dissimilarity in albedo conditions, plane of tilt and instrumentation. As the latter factors are outside the scope of this paper, they are suggested as topics for future investigations.

From the perspective of PV applications, the results indicate that PV devices with narrow SR can benefit from the generally blue rich spectral distribution in these locations, while during clear sky conditions in wintertime PV devices with wider SR can experience spectral gains. This work has been part of the COST Action PEARL PV program, which aims to improve the performance and reliability of PV systems, and where spectral data can be shared and accessed through the CKAN server in https://ckan.pearlpv-cost.eu/.

CRediT authorship contribution statement

Basant Raj Paudyal: Conceptualization, Methodology, Data analysis, Software, Writing – original draft, Writing – review & editing. **Sakthi Guhan Somasundaram:** Methodology, Data analysis, Writing – review & editing. **Atse Louwen:** Methodology, Writing – review & editing. **Angele H.M.E. Reinders:** Methodology, Writing – review & editing. **Wilfried G.J.H.M. van Sark:** Methodology, Writing – review & editing. **Dirk Stellbogen:** Methodology, Writing – review & editing. **Carolin Ulbrich:** Methodology, Writing – review & editing. **Anne Gerd Imenes:** Conceptualization, Methodology, Writing – original draft, Writing – review & editing.

Declaration of competing interest

We wish to confirm that there are no known conflicts of interest associated with this publication and there has been no significant financial support for this work that could have influenced its outcome.

We confirm that the manuscript has been read and approved by all named authors and that there are no other persons who satisfied the criteria for authorship but are not listed.

We further confirm that the order of authors listed in the manuscript has been approved by all of us. We confirm that we have given due consideration to the protection of intellectual property associated with this work and that there are no impediments to publication, including the timing of publication, with respect to intellectual property. In so doing we confirm that we have followed the regulations of our institutions concerning intellectual property.

We understand that the Corresponding Author is the sole contact for the Editorial process (including Editorial Manager and direct communications with the office). He is responsible for communicating with the other authors about progress, submissions of revisions and final approval of proofs.

Acknowledgments

The authors acknowledge the support of the COST Action PEARL-PV programme, supported by COST (European Cooperation in Science and Technology), see www.cost.eu. Basant Paudyal and Anne Gerd Imenes would like to acknowledge the support from University of Agder, Norway. Angèle Reinders would like to thank Theo Krone, Anton Driesse and the ICT department of University of Twente for their technical support. Carolin Ulbrich acknowledges support by the Helmholtz Association, Germany under the program “Energy System Design”. Atse Louwen and Wilfried van Sark would like to thank Anne de Waal (UU) for technical support, and Stichting Technologische Wetenschappen (FLASH Perspectief programme, project number 12172) for financial support.

Appendix

See Table 5.

Table 5
Input data for reference solar spectrum generation using SMARTS 2.9.2.

Card ID	Value	Parameter description
1	IEC 60904-3:2016	Header
2	1	Pressure input mode: ISPR
2a	1013.25 0	Station pressure and altitude: SPR, ALT
3	1	Standard atmosphere profile selection: IATM1
3a	USSA	Default standard atmosphere profile: ATM
4	1	Water vapor input: IH2O
5	1	Ozone calculation: IO3
6	1	Pollution level mode: IGAS
7	370	Carbon dioxide volume mixing ratio: qCO2
7a	1	Extraterrestrial spectrum: ISPCTR
8	S&F RURAL	Aerosol profile to use: AEROS
9	0	Specification for aerosol optical depth: ITURB
9a	0.084	Aerosol optical depth at 500 nm: TAU5

(*continued on next page*)

Table 5 (*continued*).

Card ID	Value	Parameter description
10	38	Far field spectral albedo file to use: IALBDX
10b	1	Specify tilt calculation: ITILT
10c	38 37 180	Albedo file to use for near field, tilt, and azimuth: IALBDG, TILT, WAZIM
11	280 4000 1.0 1367.0	Wavelength range-start, stop, mean radius vector correction, integrated solar spectrum irradiance: WLMN, WLMX, SUNCOR, SOLARC
12	2	Separate spectral output file print mode: IPRT
12a	280 4000 0.5	Output file wavelength-print limits, start, stop, minimum step size: WPMN, WPMX, INTVL
12b	1	Number of output variables to print: IOTOT
12c	8 or 2	Code relating output variables to print: OUT
13	1	Circumsolar calculation mode: ICIRC
13a	0 2.9 0	Receiver geometry-Slope, view, limit half angles: SLOPE, APERT, LIMIT
14	0	Smooth function mode: ISCAN
15	0	Illuminance calculation mode: ILLUM
16	0	UV calculation mode: IUV
17	2	Solar geometry mode: IMASS
17a	1.5	Air mass value: AMASS

References

[1] Christian A. Gueymard, Solar radiation spectrum, in: Solar Energy, Springer, 2013, pp. 608–633.

[2] IEC, Photovoltaic (pv) module performance testing and energy rating, 2011.

[3] C. Riordan, R. Hulstron, What is an air mass 1.5 spectrum? (solar cell performance calculations), in: IEEE Conference on Photovoltaic Specialists, Vol. 2, 1990, pp. 1085–1088.

[4] A. Louwen, A.C De Waal, R.E.I. Schropp, A.P.C. Faaij, W.G.J.H.M. Van Sark, Comprehensive characterisation and analysis of PV module performance under real operating conditions, Prog. Photovolt. 25 (2017) 218–232.

[5] Koichi Nakayama, Masaki Tsuji, Jakapan Chantana, Yu Kawano, Takahito Nishimura, Yoshihiro Hishikawa, Takashi Minemoto, Description of short circuit current of outdoor photovoltaic modules by multiple regression analysis under various solar irradiance levels, Renew. Energy 147 (2020) 895–902.

[6] Takashi Minemoto, Shingo Nagae, Hideyuki Takakura, Impact of spectral irradiance distribution and temperature on the outdoor performance of amorphous Si photovoltaic modules, Sol. Energy Mater. Sol. Cells 91 (10) (2007) 919–923.

[7] Daniela Dirnberger, Björn Müller, Christian Reise, PV module energy rating: opportunities and limitations, Prog. Photovolt., Res. Appl. 23 (12) (2015) 1754–1770.

[8] R. Gottschalg, T.R. Betts, D.G. Infield, M.J. Kearney, On the importance of considering the incident spectrum when measuring the outdoor performance of amorphous silicon photovoltaic devices, Meas. Sci. Technol. 15 (2) (2004) 460–466.

[9] Daniela Dirnberger, Gina Blackburn, Björn Müller, Christian Reise, On the impact of solar spectral irradiance on the yield of different PV technologies, Sol. Energy Mater. Sol. Cells 132 (2015) 431–442.

[10] DB Magare, OS Sastry, R Gupta, TR Betts, R Gottschalg, A Kumar, B Bora, YK Singh, Effect of seasonal spectral variations on performance of three different photovoltaic technologies in India, Int. J. Energy Environ. Eng. 7 (1) (2016) 93–103.

[11] Martin A. Green, Ewan D. Dunlop, Jochen Hohl-Ebinger, Masahiro Yoshita, Nikos Kopidakis, Karsten Bothe, David Hinken, Michael Rauer, Xiaojing Hao, Solar cell efficiency tables (version 60), Prog. Photovolt., Res. Appl. 30 (7) (2022) 687–701.

[12] C Ulbrich, C Zahren, A Gerber, B Blank, T Merdzhanova, A Gordijn, U Rau, Matching of silicon thin-film tandem solar cells for maximum power output, Int. J. Photoenergy 2013 (2013).

[13] Geoffrey S. Kinsey, Nicholas C. Riedel-Lyngskær, Alonso-Abella Miguel, Matthew Boyd, Marília Braga, Chunhui Shou, Raul R. Cordero, Benjamin C. Duck, Christopher J. Fell, Sarah Feron, George E. Georghiou, Nicholas Habryl, Jim J. John, Nipon Ketjoy, Gabriel López, Atse Louwen, Elijah Loyiso Maweza, Takashi Minemoto, Ankit Mittal, Cécile Molto, Guilherme Neves, Gustavo Nofuentes Garrido, Matthew Norton, Basant R. Paudyal, Enio Bueno Pereira, Yves Poissant, Lawrence Pratt, Qu Shen, Thomas Reindl, Marcus Rennhofer, Carlos D. Rodríguez-Gallegos, Ricardo Rüther, Wilfried van Sark, Miguel A. Sevillano-Bendezú, Hubert Seigneur, Jorge A. Tejero, Marios Theristis, Jan A. Töfflinger, Carolin Ulbrich, Waldeir Amaral Vilela, Xiangao Xia, Márcia A. Yamasoe, Impact of measured spectrum variation on solar photovoltaic efficiencies worldwide, Renew. Energy 196 (2022) 995–1016.

[14] T.R. Betts, C.N. Jardine, R. Gottschalg, D.G. Infield, K. Lane, Impact of spectral effects on the electrical parameters of multijunction amorphous silicon cells, in: 3rd World Conference on Photovoltaic Energy Conversion, 2003. Proceedings of, Vol. 2, 2003, pp. 1756–1759, Vol.2.

[15] R. Gottschalg, D.G. Infield, M.J. Kearney, Experimental study of variations of the solar spectrum of relevance to thin film solar cells, Sol. Energy Mater. Sol. Cells 79 (4) (2003) 527–537.

[16] Shingo Nagae, Masanori Toda, Takashi Minemoto, Hideyuki Takakura, Yoshihiro Hamakawa, Evaluation of the impact of solar spectrum and temperature variations on output power of silicon-based photovoltaic modules, Sol. Energy Mater. Sol. Cells 90 (20) (2006) 3568–3575.

[17] Takashi Minemoto, Shunichi Fukushige, Hideyuki Takakura, Difference in the outdoor performance of bulk and thin-film silicon-based photovoltaic modules, Sol. Energy Mater. Sol. Cells 93 (6) (2009) 1062–1065, 17th International Photovoltaic Science and Engineering Conference.

[18] Takashi Minemoto, Yasuhito Nakada, Hiroaki Takahashi, Hideyuki Takakura, Uniqueness verification of solar spectrum index of average photon energy for evaluating outdoor performance of photovoltaic modules, Sol. Energy 83 (8) (2009) 1294–1299.

[19] Tetsuyuki Ishii, Kenji Otani, Takumi Takashima, Effects of solar spectrum and module temperature on outdoor performance of photovoltaic modules in round-robin measurements in Japan, Prog. Photovolt., Res. Appl. 19 (2) (2011) 141–148.

[20] Tetsuyuki Ishii, Kenji Otani, Akihiko Itagaki, Kenji Utsunomiya, A simplified methodology for estimating solar spectral influence on photovoltaic energy yield using average photon energy, Energy Sci. Eng. 1 (1) (2013) 18–26.

[21] J.Y. Ye, T. Reindl, A.G. Aberle, T.M. Walsh, Effect of solar spectrum on the performance of various thin-film PV module technologies in tropical Singapore, IEEE J. Photovolt. 4 (5) (2014) 1268–1274.

[22] Cristina Cornaro, Angelo Andreotti, Influence of average photon energy index on solar irradiance characteristics and outdoor performance of photovoltaic modules, Prog. Photovolt., Res. Appl. 21 (5) (2013) 996–1003.

[23] G. Nofuentes, B. García-Domingo, J.V. Muñoz, F. Chenlo, Analysis of the dependence of the spectral factor of some PV technologies on the solar spectrum distribution, Appl. Energy 113 (2014) 302–309.

[24] M. Alonso-Abella, F. Chenlo, G. Nofuentes, M. Torres-Ramírez, Analysis of spectral effects on the energy yield of different PV (photovoltaic) technologies: The case of four specific sites, Energy 67 (2014) 435–443.

[25] Jesús Polo, Miguel Alonso-Abella, Jose A. Ruiz-Arias, José L. Balenzategui, Worldwide analysis of spectral factors for seven photovoltaic technologies, Sol. Energy 142 (2017) 194–203.

[26] Christian A. Gueymard, Interdisciplinary applications of a versatile spectral solar irradiance model: A review, Energy 30 (9) (2005) 1551–1576, Measurement and Modelling of Solar Radiation and Daylight- Challenges for the 21st Century.

[27] Pedro M. Rodrigo, Eduardo F. Fernández, Florencia M. Almonacid, Pedro J. Pérez-Higueras, Quantification of the spectral coupling of atmosphere and photovoltaic system performance: Indexes, methods and impact on energy harvesting, Sol. Energy Mater. Sol. Cells 163 (2017) 73–90.

[28] Naoya Kataoka, Shota Yoshida, Seiya Ueno, Takashi Minemoto, Evaluation of solar spectral irradiance distribution using an index from a limited range of the solar spectrum, Curr. Appl. Phys. 14 (5) (2014) 731–737.

[29] Hiroyuki Mano, Md Mijanur Rahman, Aika Kamei, Takashi Minemoto, Impact estimation of average photon energy from two spectrum bands on short circuit current of photovoltaic modules, Sol. Energy 155 (2017) 1300–1305.

[30] Masaki Tsuji, Md Mijanur Rahman, Yoshihiro Hishikawa, Kensuke Nishioka, Takashi Minemoto, Uniqueness verification of solar spectrum obtained from three sites in Japan based on similar index of average photon energy, Sol. Energy 173 (2018) 89–96.

[31] G. Nofuentes, C.A. Gueymard, J. Aguilera, M.D. Pérez-Godoy, F. Charte, Is the average photon energy a unique characteristic of the spectral distribution of global irradiance? Sol. Energy 149 (2017) 32–43.

[32] V. Louwen, A.C. de Waal, W.G.J.H.M. van Sark, Evaluation of different indicators for representing solar spectra, in: Prodeedings 43rd IEEE PV Specialist Conference, 2016, pp. 113–137.

[33] Basant Raj Paudyal, Anne Gerd Imenes, Analysis of spectral irradiance distribution for PV applications at high latitude, in: 2020 47th IEEE Photovoltaic Specialists Conference, PVSC, 2020, pp. 1834–1841.

[34] José L. Balenzategui, Fernando Fabero, José P. Silva, Solar radiation measurement and solar radiometers, in: Jesus Polo, Luis Martin-Pomares, Antonio Sanfilippo (Eds.), Solar Resources Mapping, Springer, 2019, pp. 15–69.

[35] R.R. Cordero, G. Seckmeyer, A. Damiani, J. Jorquera, J. Carrasco, R. Muñoz, L. Da Silva, F. Labbe, D. Laroze, Aerosol effects on the UV irradiance in Santiago de Chile, Atmos. Res. 149 (2014) 282–291.
[36] Yuqin Zong, Steven W Brown, B Carol Johnson, Keith R Lykke, Yoshi Ohno, Simple spectral stray light correction method for array spectroradiometers, Appl. Opt. 45 (6) (2006) 1111–1119.
[37] Tadashi Kato, Yanqun Xue, Takeshi Aoshima, Toshikazu Hasegawa, Development of a broadband spectroradiometer, in: 2008 33rd IEEE Photovoltaic Specialists Conference, IEEE, 2008, pp. 1–4.
[38] A Habte, A Andreas, L Ottoson, C Gueymard, G Fedor, S Fowler, J Peterson, R Naranen, T Kobashi, A Akiyama, et al., Indoor and Outdoor Spectroradiometer Intercomparison for Spectral Irradiance Measurement, Technical Report, National Renewable Energy Lab.(NREL), Golden, CO (United States), 2014.
[39] Roberto Galleano, Willem Zaaiman, Diego Alonso-Alvarez, Alessandro Minuto, Nicoletta Ferretti, Raffaele Fucci, Mauro Pravettoni, Martin Halwachs, Matthias Friederichs, Fabian Plag, et al., Results of the fifth international spectroradiometer comparison for improved solar spectral irradiance measurements and related impact on reference solar cell calibration, IEEE J. Photovolt. 6 (6) (2016) 1587–1597.
[40] C.R. Osterwald, K.A. Emery, D.R. Myers, C.J. Riordan, Extending the spectral range of silicon-based direct-beam solar spectral radiometric measurements, in: Conference Record of the Twentieth IEEE Photovoltaic Specialists Conference, Vol. 2, 1988, pp. 1246–1250.
[41] V Tatsiankou, K Hinzer, J Haysom, H Schriemer, K Emery, R Beal, Design principles and field performance of a solar spectral irradiance meter, Sol. Energy 133 (2016) 94–102.
[42] V. Tatsiankou, K. Hinzer, H. Schriemer, P. McVey-White, R. Beal, Efficient, real-time global spectral and broadband irradiance acquisition, in: 2018 IEEE 7th World Conference on Photovoltaic Energy Conversion (WCPEC) (A Joint Conference of 45th IEEE PVSC, 28th PVSEC 34th EU PVSEC), 2018, pp. 2362–2365.
[43] Viktar Tatsiankou, Karin Hinzer, Henry Schriemer, Joan Haysom, Richard Beal, A novel instrument for cost-effective and reliable measurement of solar spectral irradiance, in: 2015 IEEE 42nd Photovoltaic Specialist Conference, PVSC, IEEE, 2015, pp. 1–4.
[44] Marcel Šúri, Thomas A. Huld, Ewan D. Dunlop, Heinz A. Ossenbrink, Potential of solar electricity generation in the European union member states and candidate countries, Sol. Energy 81 (10) (2007) 1295–1305.
[45] COST ACTION PEARL PV.
[46] Deliang Chen, Hans Weiteng Chen, Using the Köppen classification to quantify climate variation and change: An example for 1901–2010, Environ. Dev. 6 (2013) 69–79.
[47] W.G.J.H.M. Van Sark, A. Louwen, A.C. de Waal, R.E.I. Schropp, UPOT: the utrecht photovoltaic outdoor test facility, in: Proceedings of the 27th European Photovoltaic Solar Energy Conference, 2012, pp. 3247–3249.
[48] M. Norton, A.M. Gracia Amillo, R. Galleano, Comparison of solar spectral irradiance measurements using the average photon energy parameter, Sol. Energy 120 (2015) 337–344.
[49] Christian A. Gueymard, The SMARTS spectral irradiance model after 25 years: New developments and validation of reference spectra, Sol. Energy 187 (2019) 233–253.
[50] Fritz Kasten, Andrew T. Young, Revised optical air mass tables and approximation formula, Appl. Opt. 28 (22) (1989) 4735–4738.
[51] William F. Holmgren, Clifford W. Hansen, Mark A. Mikofski, Pvlib python: a python package for modeling solar energy systems, J. Open Source Softw. 3 (29) (2018) 884.
[52] G. Kopp, Science highlights and final updates from 17 years of total solar irradiance measurements from the solar radiation and climate experiment/total irradiance monitor (SORCE/TIM), Sol. Phys. 296 (2021).
[53] Manajit Sengupta, Yu Xie, Anthony Lopez, Aron Habte, Galen Maclaurin, James Shelby, The national solar radiation data base (NSRDB), Renew. Sustain. Energy Rev. 89 (2018) 51–60.
[54] Stephen E. Schwartz, Peter R. Buseck, Absorbing phenomena, Science 288 (5468) (2000) 989–990.
[55] U. Lohmann, J. Feichter, Global indirect aerosol effects: a review, Atmos. Chem. Phys. 5 (3) (2005) 715–737.
[56] R.B.A. Koelemeijer, C.D. Homan, J. Matthijsen, Comparison of spatial and temporal variations of aerosol optical thickness and particulate matter over europe, Atmos. Environ. 40 (27) (2006) 5304–5315.
[57] Jing Wei, Zhanqing Li, Yiran Peng, Lin Sun, MODIS collection 6.1 aerosol optical depth products over land and ocean: validation and comparison, Atmos. Environ. 201 (2019) 428–440.
[58] Eduardo F. Fernández, Florencia Almonacid Cruz, Tapas K. Mallick, Senthilarasu Sundaram, Effect of spectral irradiance variations on the performance of highly efficient environment-friendly solar cells, IEEE J. Photovolt. 5 (4) (2015) 1150–1157.
[59] Ilias Fountoulakis, Panagiotis Kosmopoulos, Kyriakoula Papachristopoulou, Ioannis-Panagiotis Raptis, Rodanthi-Elisavet Mamouri, Argyro Nisantzi, Antonis Gkikas, Jonas Witthuhn, Sebastian Bley, Anna Moustaka, Johannes Buehl, Patric Seifert, Diofantos G. Hadjimitsis, Charalampos Kontoes, Stelios Kazadzis, Effects of aerosols and clouds on the levels of surface solar radiation and solar energy in cyprus, Remote Sens. 13 (12) (2021).
[60] Agana Louisse S. Domingo, Ernest P. Macalalad, Temporal analysis of GNSS-based precipitable water vapor during rainy days over the Philippines from 2015 to 2017, Atmosphere 13 (3) (2022).
[61] Zhenhong Li, Jan-Peter Muller, Paul Cross, Comparison of precipitable water vapor derived from radiosonde, GPS, and moderate-resolution imaging spectroradiometer measurements, J. Geophys. Res.: Atmos. 108 (D20) (2003).
[62] P. Yuan, R. Van Malderen, X. Yin, H. Vogelmann, J. Awange, B. Heck, H. Kutterer, Characterizations of europe's integrated water vapor and assessments of atmospheric reanalyses using more than two decades of ground-based GPS, Atmos. Chem. Phys. Discuss. 2021 (2021) 1–38.
[63] P.A. Newman, L.D. Oman, A.R. Douglass, E.L. Fleming, S.M. Frith, M.M. Hurwitz, S.R. Kawa, C.H. Jackman, N.A. Krotkov, E.R. Nash, J.E. Nielsen, S. Pawson, R.S. Stolarski, G.J.M. Velders, What would have happened to the ozone layer if chlorofluorocarbons (CFCs) had not been regulated? Atmos. Chem. Phys. 9 (6) (2009) 2113–2128.
[64] M. Dameris, D.G. Loyola, M. Nützel, M. Coldewey-Egbers, C. Lerot, F. Romahn, M. van Roozendael, Record low ozone values over the arctic in boreal spring 2020, Atmos. Chem. Phys. 21 (2) (2021) 617–633.
[65] M. Blumthaler, W. Ambach, R. Ellinger, Increase in solar UV radiation with altitude, J. Photochem. Photobiol. B 39 (2) (1997) 130–134.
[66] RR Cordero, A Damiani, G Seckmeyer, J Jorquera, M Caballero, P Rowe, J Ferrer, R Mubarak, J Carrasco, R Rondanelli, M Matus, D Laroze, The solar spectrum in the Atacama desert, Sci. Rep. 6 (1) (2016) 22457.
[67] A. Guechi, M. Chegaar, M. Aillerie, Air mass effect on the performance of organic solar cells, Energy Procedia 36 (2013) 714–721, TerraGreen 13 International Conference 2013 - Advancements in Renewable Energy and Clean Environment.
[68] W.G.J.H.M. van Sark, A. Meijerink, R.E.I. Schropp, Nanoparticles for solar spectrum conversion, in: Loucas Tsakalakos (Ed.), Nanotechnology for Photovoltaics, CRC Press, 2010, pp. 351–390.
[69] Basant Raj Paudyal, Anne Gerd Imenes, Uniqueness verification of blue fraction as a parameter of spectral irradiance quantification, in: 2021 IEEE 48th Photovoltaic Specialists Conference, PVSC, 2021, pp. 2563–2568.
[70] Georgi Hristov Yordanov, Tor Oskar Saetre, Ole-Morten Midtgård, Extreme overirradiance events in Norway: 1.6 suns measured close to 60°N, Sol. Energy 115 (2015) 68–73.
[71] Junfang Zhang, Kota Watanabe, Jun Yoshino, Tomonao Kobayashi, Yoshihiro Hishikawa, Takuya Doi, Physical process and statistical properties of solar irradiance enhancement observed under clouds, Japan. J. Appl. Phys. 57 (8S3) (2018) 08RG11.
[72] O.V. Voziakova, Atmospheric transparency over Mount Shatdzhatmaz in the optical and near-infrared ranges, Astron. Lett. 38 (4) (2012) 271–279.
[73] Arctic Climate Impact Assessment, Arctic Climate Impact Assessment, vol. 1042, Cambridge University Press Cambridge, 2005.
[74] Yasuhito Nakada, Hiroaki Takahashi, Kyoko Ichida, Takashi Minemoto, Hideyuki Takakura, Influence of clearness index and air mass on sunlight and outdoor performance of photovoltaic modules, Curr. Appl. Phys. 10 (2, Supplement) (2010) S261–S264, The Proceeding of the International Renewable Energy Conference and Exhibition 2008 (RE2008).
[75] Ahmed Elsayed Ghitas, Studying the effect of spectral variations intensity of the incident solar radiation on the Si solar cells performance, NRIAG J. Astron. Geophys. 1 (2) (2012) 165–171.
[76] Nicholas Riedel-Lyngskær, Martynas Ribaconka, Mário Pó, Anders Thorseth, Sune Thorsteinsson, Carsten Dam-Hansen, Michael L. Jakobsen, The effect of spectral albedo in bifacial photovoltaic performance, Sol. Energy 231 (2022) 921–935.
[77] Christian A. Gueymard, et al., SMARTS code, version 2.9. 5 user's manual, Solar Consult. Serv. (2005).